D. García-González, R. Zaera, A. Arias. A hyperelastic-thermoviscoplastic constitutive model for semi-crystalline polymers: application to PEEK under dynamic loading conditions, in: *International journal of plasticity* 88 (2017), pp. 27-52
DOI: https://doi.org/10.1016/j.ijplas.2016.09.011

A hyperelastic-thermoviscoplastic constitutive model for semi-crystalline polymers: Application to PEEK under dynamic loading conditions

D. Garcia-Gonzalez*, R. Zaera, A. Arias

Department of Continuum Mechanics and Structural Analysis, University Carlos III of Madrid, Avda. de la Universidad 30, 28911 Leganés, Madrid, Spain

Keywords:
Semi-crystalline polymers
High strain rate
Temperature dependence
Large deformation
PEEK

A B S T R A C T

In this work, a hyperelastic-thermoviscoplastic constitutive model including thermo-mechanical coupling is presented to predict the mechanical behavior of semi-crystalline polymers. The constitutive model is based on the original approach developed by Polanco-Loria and coauthors (2010) and it accounts for: material hardening due to strain rate sensitivity, temperature evolution during the deformation process due to heat generation induced by plastic dissipation, thermal softening and thermal expansion of the material. The parameters of the constitutive model have been identified for polyether-ether-ketone (PEEK) from experimental data published by Rae and coauthors (2007). In order to analyze the predictive capacity of the model under dynamic conditions, the constitutive model has been implemented in a FE code within a large deformation framework to study two different problems: low velocity impact test on PEEK thin plates and dynamic necking on PEEK slender bar. These problems involve large and irreversible deformations, high strain rates and temperature increment due to plastic dissipation. The analysis determines the interplay between strain rate and thermal effects in the material behavior. The constitutive model presented herein reproduces adequately the mechanical behavior of PEEK under different thermal and loading conditions, demonstrating the importance of considering the coupling between temperature and strain rate.

1. Introduction

Due to their attractive mechanical properties, rapid processing and relatively low manufacturing cost, thermoplastic polymers are used in a large range of industrial sectors. Because of the increasing interest in, and use of, these polymers, it is fundamental to understand their behavior under different loading conditions. There are many devices employed in automotive, aeronautical and biomedical applications which are exposed to impact loading conditions. Such devices like car safety system, leading edges in aircrafts or cranial replacements can be subjected to high strain rates which result in a complex behavior. On the other hand, in the design and manufacturing process, the estimation of temperature evolution leading to thermal softening and thermal expansion is essential.

* Corresponding author.
E-mail address: danigarc@ing.uc3m.es (D. Garcia-Gonzalez).

Nomenclature

$\{\Omega_o, \overline{\Omega}, \overline{\overline{\Omega}}, \Omega\}$	initial, dilated, dilated relaxed and current configurations
$\{e, e_o, \overline{e}\}$	specific internal energy per unit volume in Ω, Ω_o and $\overline{\Omega}$
$\{\mathbf{q}, \mathbf{Q}, \overline{\mathbf{Q}}\}$	heat flux per unit volume in Ω, Ω_o and $\overline{\Omega}$
$\{r, R, \overline{R}\}$	heat source per unit volume in Ω, Ω_o and $\overline{\Omega}$
$\{\eta, \overline{\eta}\}$	specific entropy per unit volume in Ω and $\overline{\Omega}$
$\overline{C}$	heat capacity per unit volume
$\{\theta, \theta_{ref}, \theta_{melt}\}$	current, reference and melting temperature
f_θ	temperature-dependent function
$\overline{\Psi}$	Helmholtz free energy per unit volume
∇_X	gradient with respect to the material point $\mathbf{X}$ in Ω_o
∇_x	gradient with respect to the spatial point $\mathbf{x}$ in Ω
$\mathfrak{L}$	Langevin function
$\mathbf{I}$	Identity matrix
J	determinant of the deformation gradient
J^θ	determinant of the thermal deformation gradient
J^M	determinant of the mechanical deformation gradient
J_N	determinant of the network deformation gradient
J_I	determinant of the intermolecular deformation gradient
J_I^e	determinant of the intermolecular elastic deformation gradient
$\mathbf{F}$	deformation gradient
$\mathbf{F}^\theta$	thermal deformation gradient
$\{\mathbf{F}^M, \mathbf{F}_I^M, \mathbf{F}_N^M\}$	mechanical deformation gradient contributions
$\mathbf{F}_N^e$	network elastic deformation gradient
$\mathbf{F}_I^e$	intermolecular elastic deformation gradient
$\mathbf{F}_I^p$	intermolecular plastic deformation gradient
$\mathbf{C}_N^e$	network elastic right Cauchy-Green tensor
$\{\mathbf{C}_I^e, \mathbf{B}_I^e\}$	intermolecular elastic right and left Cauchy-Green tensors
$\mathbf{v}$	velocity
$\mathbf{l}$	velocity gradient
$\mathbf{l}_N^e$	network elastic velocity spatial gradient
$\mathbf{l}_I^e$	intermolecular elastic velocity spatial gradient
$\overline{\mathbf{L}}^\theta$	thermal velocity spatial gradient
$\overline{\overline{\mathbf{L}}}_I^p$	plastic velocity spatial gradient
$\mathbf{d}$	symmetric part of the velocity gradient
$\mathbf{d}_N^e$	symmetric part of the network elastic velocity gradient
$\mathbf{d}_I^e$	symmetric part of the intermolecular elastic velocity gradient
$\overline{\mathbf{D}}^\theta$	symmetric part of the thermal velocity gradient
$\overline{\overline{\mathbf{D}}}_I^p$	symmetric part of the intermolecular plastic velocity gradient
$\mathbf{w}$	skew part of the velocity gradient
$\overline{\mathbf{W}}^\theta$	skew part of the thermal velocity gradient
$\overline{\overline{\mathbf{W}}}_I^p$	skew part of the intermolecular plastic velocity gradient
$\boldsymbol{\sigma}$	Cauchy stress tensor
$\boldsymbol{\sigma}_N$	network Cauchy stress tensor
$\boldsymbol{\sigma}_I$	intermolecular Cauchy stress tensor
$\mathbf{P}$	first Piola-Kirchhoff stress tensor
$\overline{\mathbf{S}}_N$	network second Piola-Kirchhoff stress tensor
$\{\overline{\mathbf{S}}_I, \overline{\overline{\mathbf{S}}}_I\}$	intermolecular second Piola-Kirchhoff stress tensor in $\overline{\Omega}$ and $\overline{\overline{\Omega}}$
$\overline{\mathbf{M}}_N$	network Mandel stress tensor
$\{\overline{\mathbf{M}}_I, \overline{\overline{\mathbf{M}}}_I\}$	intermolecular Mandel stress tensor in $\overline{\Omega}$ and $\overline{\overline{\Omega}}$
$\overline{\lambda}$	average total stretch ratio
$\{I_{1I}, J_{2I}\}$	stress invariants of the intermolecular Mandel stress tensor
$\overline{\overline{\sigma}}_{eqI}$	Rhagava equivalent stress
g_I	plastic potential

$\bar{\bar{\mathbf{r}}}_{\mathbf{I}}$	gradient of the plastic potential
$\dot{\bar{\gamma}}^{\mathrm{P}}$	viscoplastic multiplier
α_θ	thermal expansion coefficient
$\{\lambda_0, \mu_0\}$	classical Lamé constants
E	Young's modulus
$\{E_{ref}, E_1\}$	Young's modulus at the reference temperature and a material parameter
$\{\sigma_T, \sigma_{T0}\}$	yield stress in uniaxial tension and its value at reference temperature
α	pressure sensitivity parameter
β	volumetric plastic strain parameter
$\dot{\epsilon}_{0I}$	reference strain rate
C	rate sensitivity parameter
m	temperature sensitivity parameter
C_R	initial elastic modulus of the network resistance
$\bar{\lambda}_L$	locking stretch
κ	network bulk modulus
τ	characteristic timescale

The nonlinear behavior of thermoplastic polymers reflects its time, pressure, strain rate and temperature dependencies and the coupling of viscoelastic and viscoplastic behaviors (Krairi and Doghri, 2014). In addition, their behavior becomes more complex when large deformations are reached that influence structural parameters such as crosslinking, molecular weights and crystallinity degree (Ayoub et al., 2010). Particularly relevant is the consideration of thermal and strain rate effects on the material behavior. There is a strong relationship between thermoplastic polymers behavior and temperature, with thermal softening as the temperature increases. In addition, the yielding and plastic flow behaviors are influenced by strain rate resulting in a loss in ductility and a continuous hardening as strain rate increases (Rae et al., 2007; Serban et al., 2013; El-Qoubaa and Othman, 2016). This relationship becomes more complex at high strain rates of deformation where material hardening, induced by strain rate effects, is in competition with the significant thermal softening induced by adiabatic heating (Mohagheghian et al., 2015). This coupling between the thermal and mechanical behavior of thermoplastic polymers also affects the relaxation or transition temperatures at which the material suddenly changes its behavior (Gaymans et al., 2000; Jordan et al., 2007; Srivastava et al., 2010; Nasraoui et al., 2012). The transition temperatures delimit the different behavior regions, highlighting the glass transition and the beta transition, which are related to a ductile-to-brittle change in the material behavior (Gaymans et al., 2000; Garcia-Gonzalez et al., 2015a).

The complicated behavior of thermoplastic polymers makes it challenging to predict their mechanical response and performance when designing products made from this kind of materials. Therefore, reliable models able to describe the different aspects of thermoplastic polymers behavior, including the variables which govern their mechanical response, is of both theoretical and practical interest. In these terms, the constitutive modeling of thermoplastic polymers has been widely investigated and constitutive models have been developed generally relying on two main approaches: phenomenological and physical.

Popelar et al. (2004) developed a phenomenological approach to describe the behavior of semi-crystalline polymers, proposing a nonlinear viscoelastic model based on the Schapery (1984) viscoelasticity theory. Subsequent researchers developed constitutive models including viscoplasticity (Colak and Dusunceli, 2006; Zaïri et al., 2008). Halabi et al. (2011) applied a homogenized phenomenological model to study thermoplastic cranial implants and more recently, phenomenological approaches, based on models developed for metal, have been used to consider the viscoplastic behavior of thermoplastic polymers (Louche et al., 2009; Garcia-Gonzalez et al., 2015b, 2015c; El-Qoubaa and Othman, 2016).

The physical approaches introduce features of the microstructure in the mathematical development of the constitutive model. The physical assumptions take into account two key factors: firstly the crystalline regions in the microstructure which govern the material response in the early stages of deformation; and secondly the amorphous phase during which plastic deformation is related to relative movements between the molecule chains that control the later stages of deformation. In this regard, models developed for amorphous polymers can be employed to define the amorphous regions in semi-crystalline polymers. Haward and Thackray (1968) proposed a one-dimensional description incorporating both yielding and strain hardening; and numerous researchers proposed three-dimensional models inspired by the latter (Boyce et al., 1988; Arruda and Boyce, 1993; Wu and van der Giessen, 1995; Ayoub et al., 2010). Mulliken and Boyce (2006) proposed a model which captures the transition in the yield behavior and also predict the post-yield large strain behavior. Based on this approach, Sarva et al. (2007) studied the impact behavior of polycarbonate considering large strain rate-dependent elastic-viscoplasticity. More recently, Polanco-Loria et al. (2010) developed a hyperelastic-viscoplastic material model for semi-crystalline polymers which includes pressure dependence, volumetric plastic strain and strain-rate sensitivity. Following the thermo-mechanical constitutive models of amorphous polymers (Boyce and Arruda, 2000; Srivastava et al., 2010; Billon, 2012) and the non-gaussian statistic approach of entangled polymer network (Edwards and Vilgis, 1986), Maurel-Pantel et al. (2015) developed a thermo-mechanical large deformation constitutive approach for semi-crystalline polymers.

In relation to semi-crystalline polymers, despite the abundant literature on their mechanical behavior under isothermal conditions, only a few studies focus on thermomechanical modeling and these are limited to loading tests where low strain

rate values are reached (Bergström et al., 2003; Maurel-Pantel et al., 2015). Moreover, there is a critical strain rate at which the system is expected to behave adiabatically depending on thermal properties and loading conditions (Kendall and Siviour, 2013; Kendall and Siviour, 2014). This effect introduces a change in the material behavior related to the temperature increment due to plastic dissipation and the associated thermal softening. The thermomechanical coupling must be taken into account by the constitutive model to obtain successful results in dynamic conditions. This consideration is especially relevant at high strain rates where plastic mechanical deformation leads to important local temperature increases.

The objective of this paper is to provide a constitutive model which takes into account thermal softening, strain rate and pressure sensitivities and temperature evolution. The model follows the formulation proposed by Polanco-Loria et al. (2010), who developed their model assuming isothermal conditions. Moreover, the formulation has been developed under the assumptions of large deformation within a thermomechanical framework. The constitutive model developed herein allows for predicting the mechanical behavior of semi-crystalline polymers not only under isothermal assumptions but also providing the evolution of temperature due to plastic dissipation, being this one of the key contributions of the present work. This point is quite relevant since at high strain rates the change in temperature due to adiabatic heating can lead to important changes in the polymer behavior. These changes in the deformation mechanisms are controlled by transition temperatures and, therefore, the temperature prediction provided by the model is essential for evaluating if the material is working between the ductile-to-brittle and the glass transition temperatures. This is an important point since these polymers show a considerable loss in ductility and increase in stiffness and yield stress below their ductile-to-brittle temperature. In the case of exceeding the glass transition temperature, they show a marked reduction in stiffness and yield stress and also an increase in ductility. The constitutive model presented herein provides reliable predictions from the ductile-to-brittle transition until the glass transition, the temperature range within the assumptions of the model are valid.

The model has been applied to describe the behavior of the semi-crystalline polymer polyether-ether-ketone (PEEK) in a wide range of strain rates and testing temperatures. Its parameters have been identified from experimental data of uniaxial compression and tensile tests published by Rae et al. (2007). In order to analyze the predictive capacity under dynamic conditions, the model has been implemented in a FE code to study two different problems: low velocity impact test on PEEK thin plates and dynamic necking on PEEK slender bar. In addition, both dynamic applications determine the interplay between strain rate and thermal effects and demonstrate the capacity of the model to analyze the thermomechanical behavior of semi-crystalline polymers.

2. Description of the constitutive model

According to different authors (Haward and Thackray, 1968; Boyce et al., 2000), the stress-strain behavior for thermoplastic polymers can be interpreted as a response to overcoming two basic forms of resistances to deformation:

- Intermolecular resistance (I): an intermolecular barrier to deformation which is increased by the development of strain-induced crystallization.
- Network resistance (N): an entropic resistance caused by molecular orientation.

The intermolecular resistance is taken to increase due to the strain-induced crystallization and results in the initially stiff behavior as well as the rate and temperature dependence of initial flow. The network resistance resulting from molecular alignment provokes the strain hardening/stiffening behavior. Based on the additive definition of stress state understood as the combination of both resistance contributions, Polanco-Loria et al. (2010) developed a constitutive model restricted to isothermal conditions. The Polanco-Loria model can exhibit a limitation when, upon the deformation process, a temperature variation is expected. However, the present model takes into account not only the material hardening due to strain rate effects but also its coupling with thermal effects which results in a competition between hardening due to strain rate sensitivity and softening due to temperature sensitivity. This effect is especially relevant for semi-crystalline polymers which exhibit a strong dependence of their mechanical behavior on temperature. Specifically under dynamic conditions, plastic dissipation can cause a considerable temperature increase.

The work presented herein proposes a hyperelastic-thermoviscoplastic material model which takes into account thermomechanical coupling. The additive definition of stress state as the combination of resistance contributions under isothermal or adiabatic conditions, (Fig. 1a), allows us to configure the rheological scheme of the constitutive model, (Fig. 1b). The rate and temperature-dependent part (*Intermolecular resistance*, denoted by I) is taken to originate from an intermolecular barrier to deformation. A Neo-Hookean hyperelastic model was selected for describing the elastic spring characterizing the initial elastic contribution due to internal energy change, denoted by I_1. The thermoviscoplastic behavior is taken into account by a nonlinear viscoplastic dashpot capturing the rate and temperature dependent behavior of the material. This component has been defined in parallel to a friction element which activates the nonlinear viscoplastic dashpot when a yield function is satisfied. In this regard, the constitutive elements must be understood as a physically motivated choice but not as a faithful representation of the polymer microstructural response. The set of elements composed by the nonlinear viscoplastic dashpot and the friction element is denoted by I_2 and defines the shape of the thermoviscoplastic contribution to the intermolecular resistance stress-strain curve. The equilibrium part of the stress-strain behavior (*Network resistance*, denoted by N) acts as the backbone of the overall material stress-strain behavior and originates from an evolving entropic resistance

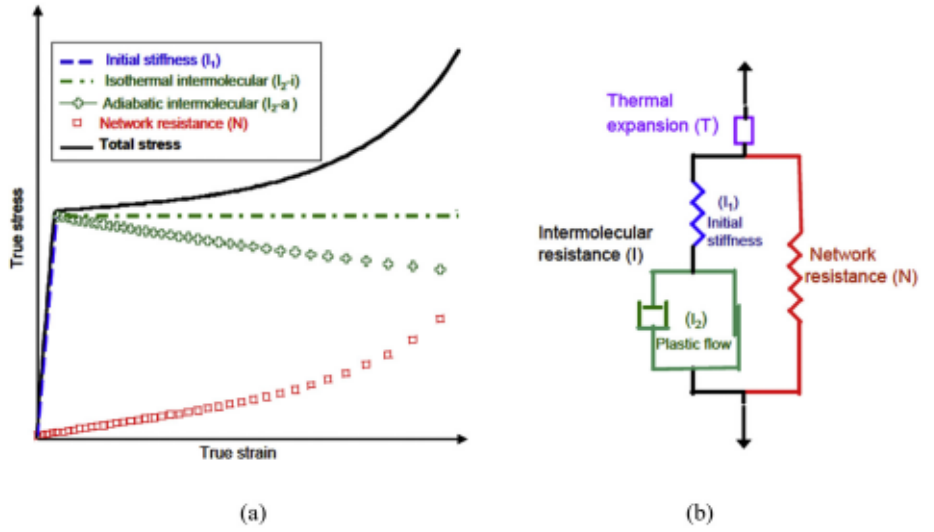

(a) (b)

Fig. 1. (a) Stress contributions from intermolecular and network resistances and their decompositions; (b) rheological scheme of the present constitutive model.

due to molecular orientation. This part is composed of a unique spring which implies a purely elastic contribution to the stress-strain behavior. Moreover, *thermal expansion* is taken into account by the addition of an element denoted by T. Details of constitutive relations defining each element will be given next.

2.1. Kinematics

As shown in Fig. 2, four configurations have been established in order to define the kinematics of the model, going from an initial reference configuration Ω_o to a final loaded or current configuration Ω. Two intermediate configurations have been added allowing us to define the constitutive equations of both branches of the model. The first one is referred to as a dilated configuration $\overline{\Omega}$ in which only thermal deformation is accounted for, and the second one is referred to as a dilated relaxed configuration $\overline{\overline{\Omega}}$ in which both thermal and plastic deformations are considered.

Taking $\mathbf{X}$ as an arbitrary material point in the undeformed or reference configuration Ω_o, it is possible to reach the current configuration Ω, through the mapping $\mathbf{x} = \chi(\mathbf{X},t)$, from which the deformation gradient ($\mathbf{F}$), velocity ($\mathbf{v}$) and velocity gradient ($\mathbf{l}$) can be derived as

$$\mathbf{F} = \nabla_X \chi; \mathbf{v} = \dot{\chi}; \mathbf{l} = \nabla_x \mathbf{v} = \dot{\mathbf{F}}\mathbf{F}^{-1} \tag{1}$$

respectively, where ∇_x denotes the material gradient and ∇_x denotes the spatial gradient.

A multiplicative split is used to break down the deformation gradient into thermal, $\mathbf{F}^{\theta}$, and mechanical, $\mathbf{F}^{\mathbf{M}}$, parts (Yu et al., 1997; Kamlah and Tsakmakis, 1999; Lion, 2000; Li and Xu, 2011; Chen et al., 2014; Ge et al., 2014)

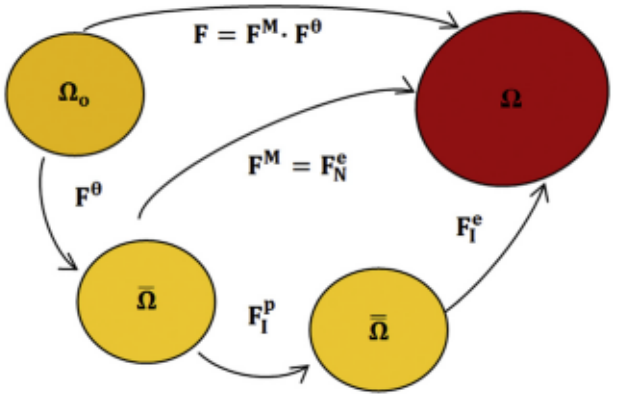

Fig. 2. Kinematics of the model showing the reference or initial configuration Ω_o, the dilated configuration $\overline{\Omega}$, the dilated relaxed configuration $\overline{\overline{\Omega}}$, and the current or loaded configuration Ω.

$$\mathbf{F} = \mathbf{F}^{\mathbf{M}}\mathbf{F}^{\theta} \tag{2}$$

The mechanical part of the deformation gradient, $\mathbf{F}^{\mathbf{M}}$, is equivalent to the intermolecular resistance, $\mathbf{F}_{\mathbf{I}}^{\mathbf{M}}$, and to the network resistance, $\mathbf{F}_{\mathbf{N}}^{\mathbf{M}}$, according to the rheological model

$$\mathbf{F}^{\mathbf{M}} = \mathbf{F}_{\mathbf{I}}^{\mathbf{M}} = \mathbf{F}_{\mathbf{N}}^{\mathbf{M}} \tag{3}$$

Thus, the same volume change represented by the Jacobian, J^{M}, has been associated with both mechanical parts of the model given as the determinant of each part of the deformation gradient

$$J^{M} = J_{I} = J_{N} = \det\left(\mathbf{F}^{\mathbf{M}}\right) \tag{4}$$

where J_I is the Jacobian associated with intermolecular resistance and J_N is the Jacobian associated with network resistance. The total volume change can be represented by the total Jacobian composed of both mechanical and thermal contributions

$$J = J^{M}J^{\theta} = \det(\mathbf{F}) \tag{5}$$

The mechanical deformation gradient of network resistance is defined as purely elastic, $\mathbf{F}_{\mathbf{N}}^{\mathbf{M}} = \mathbf{F}_{\mathbf{N}}^{\mathbf{e}}$. The intermolecular resistance describes the thermoviscoplastic response of the material. The deformation gradient $\mathbf{F}_{\mathbf{I}}^{\mathbf{M}}$ can be decomposed into the component $\mathbf{F}_{\mathbf{I}_1}^{\mathbf{M}}$ associated with the Neo-Hookean hyperelastic spring and the component $\mathbf{F}_{\mathbf{I}_2}^{\mathbf{M}}$ associated with the nonlinear viscoplastic dashpot (Kroner, 1960; Lee, 1969).

$$\mathbf{F}_{\mathbf{I}}^{\mathbf{M}} = \mathbf{F}_{\mathbf{I}_1}^{\mathbf{M}}\mathbf{F}_{\mathbf{I}_2}^{\mathbf{M}} \tag{6}$$

The kinematics of the model can be defined in terms of the deformation gradient decomposition for the intermolecular resistance as

$$\mathbf{F}_{\mathbf{I}_1}^{\mathbf{M}} = \mathbf{F}_{\mathbf{I}}^{\mathbf{e}} \tag{7}$$

$$\mathbf{F}_{\mathbf{I}_2}^{\mathbf{M}} = \mathbf{F}_{\mathbf{I}}^{\mathbf{p}} \tag{8}$$

where $\mathbf{F}_{\mathbf{I}}^{\mathbf{e}}$ represents the elastic part due to reversible elastic mechanisms of the intermolecular resistance, and $\mathbf{F}_{\mathbf{I}}^{\mathbf{p}}$ represents the inelastic part due to irreversible mechanisms.

Combining Eqs. (2) (3) and (6) makes it possible to obtain the following expression for the total deformation gradient

$$\mathbf{F} = \mathbf{F}_{\mathbf{I}}^{\mathbf{e}}\mathbf{F}_{\mathbf{I}}^{\mathbf{p}}\mathbf{F}^{\theta} = \mathbf{F}_{\mathbf{N}}^{\mathbf{e}}\mathbf{F}^{\theta} \tag{9}$$

where $\mathbf{F}_{\mathbf{N}}^{\mathbf{e}}$ represents the elastic part due to reversible elastic mechanisms of the network resistance. The intermediate dilated configuration $\overline{\Omega}$, can be obtained from Ω by mapping through $\mathbf{F}^{-\mathbf{M}}$. In case of the dilated relaxed configuration $\overline{\overline{\Omega}}$, it can be obtained from Ω by mapping through $\mathbf{F}_{\mathbf{I}}^{-\mathbf{e}}$.

The velocity gradient $\mathbf{l}$, in terms of the kinematics associated with the intermolecular resistance elements, can be written using Eq. (9) as

$$\mathbf{l} = \dot{\mathbf{F}}\mathbf{F}^{-1} = \mathbf{l}_{\mathbf{I}}^{\mathbf{e}} + \mathbf{F}_{\mathbf{I}}^{\mathbf{e}}\overline{\overline{\mathbf{L}}}_{\mathbf{I}}^{\mathbf{p}}\mathbf{F}_{\mathbf{I}}^{-\mathbf{e}} + \mathbf{F}_{\mathbf{I}}^{\mathbf{e}}\mathbf{F}_{\mathbf{I}}^{\mathbf{p}}\overline{\mathbf{L}}^{\theta}\mathbf{F}_{\mathbf{I}}^{-\mathbf{p}}\mathbf{F}_{\mathbf{I}}^{-\mathbf{e}} \tag{10}$$

where $\mathbf{l}_{\mathbf{I}}^{\mathbf{e}} = \dot{\mathbf{F}}_{\mathbf{I}}^{e}\mathbf{F}_{\mathbf{I}}^{-\mathbf{e}}$ is the elastic component of the velocity gradient in the current configuration, $\overline{\mathbf{L}}^{\theta} = \dot{\mathbf{F}}^{\theta}\mathbf{F}^{-\theta}$ is the thermal component of the velocity gradient in the dilated configuration and the plastic component $\overline{\overline{\mathbf{L}}}_{\mathbf{I}}^{\mathbf{p}}$ can be defined in the dilated relaxed configuration $\overline{\overline{\Omega}}$ as

$$\overline{\overline{\mathbf{L}}}_{\mathbf{I}}^{\mathbf{p}} = \dot{\mathbf{F}}_{I}^{\mathbf{p}}\mathbf{F}_{\mathbf{I}}^{-\mathbf{p}} \tag{11}$$

This velocity gradient can be decomposed into its symmetric and skew parts by $\overline{\overline{\mathbf{L}}}_{\mathbf{I}}^{\mathbf{p}} = \overline{\overline{\mathbf{D}}}_{\mathbf{I}}^{\mathbf{p}} + \overline{\overline{\mathbf{W}}}_{\mathbf{I}}^{\mathbf{p}}$. In this work, $\overline{\overline{\Omega}}$ is assumed to be invariant to the rigid body rotations of the current configuration, that is $\overline{\overline{\mathbf{W}}}_{\mathbf{I}}^{\mathbf{p}} = 0$, and therefore $\overline{\overline{\mathbf{D}}}_{\mathbf{I}}^{\mathbf{p}} = \overline{\overline{\mathbf{L}}}_{\mathbf{I}}^{\mathbf{p}}$ (Boyce et al., 1988; Gurtin and Anand, 2005). Regarding the thermal component of the velocity gradient, it can be also decomposed

into its symmetric and asymmetric parts by $\overline{\mathbf{L}}^{\theta} = \overline{\mathbf{D}}^{\theta} + \overline{\mathbf{W}}^{\theta}$. According to Bouvard et al. (2013), the thermal contribution to the deformation gradient is assumed to be isotropic. Therefore, $\mathbf{F}^{\theta}$ is spheric and it is possible to assume $\overline{\mathbf{W}}^{\theta} = 0$.

The total velocity gradient can be likewise defined through the kinematics of the network resistance using Eq. (9) as

$$\mathbf{l} = \dot{\mathbf{F}}\bar{\mathbf{F}}^{-1} = \mathbf{l}_{\mathbf{N}}^{\mathbf{e}} + \mathbf{F}_{\mathbf{N}}^{\mathbf{e}}\bar{\mathbf{L}}^{\theta}\bar{\mathbf{F}}_{\mathbf{N}}^{\mathbf{e}} \tag{12}$$

where $\mathbf{l}_{\mathbf{N}}^{\mathbf{e}} = \dot{\mathbf{F}}_{\mathbf{N}}^{\mathbf{e}}\bar{\mathbf{F}}_{\mathbf{N}}^{\mathbf{e}}$.

2.2. Decomposition of stress

According to the stress decomposition shown in Fig. 1 (left) and the arrangement of the rheological model elements depicted in Fig. 1 (right), the total stress is determined by the contribution of the intermolecular and the network resistances. The total Cauchy stress $\boldsymbol{\sigma}$ in the polymer is given by the sum of the Cauchy stresses of the intermolecular resistance $\boldsymbol{\sigma}_{\mathbf{I}}$ and the network resistance $\boldsymbol{\sigma}_{\mathbf{N}}$

$$\boldsymbol{\sigma} = \boldsymbol{\sigma}_{\mathbf{I}} + \boldsymbol{\sigma}_{\mathbf{N}} \tag{13}$$

where the contribution of the intermolecular resistance $\boldsymbol{\sigma}_{\mathbf{I}}$ is equal to both the Cauchy stress $\boldsymbol{\sigma}_{\mathbf{I}_1}$ associated with the Neo-Hookean hyperelastic spring and the Cauchy stress $\boldsymbol{\sigma}_{\mathbf{I}_2}$ associated with the nonlinear viscoplastic dashpot in parallel with the friction element

$$\boldsymbol{\sigma}_{\mathbf{I}} = \boldsymbol{\sigma}_{\mathbf{I}_1} = \boldsymbol{\sigma}_{\mathbf{I}_2} \tag{14}$$

The spring of the intermolecular resistance provides the initial stiffness and therefore the initial slope of the stress-strain curve depending on temperature. Once the yield stress is reached, the contribution of the dashpot starts which introduces a temperature softening if temperature increases. At the same time, the model takes into account the contribution of the spring presented in the network resistance which describes a hyperelastic entropic resistance originally proposed as the eight chain model by Arruda and Boyce (1993). This model determines the network response considering eight orientations of principal stretch space, allowing it to simulate a true network response of cooperative chain stretching.

2.3. Thermodynamics

In this section, the thermodynamic consistency of the model is imposed by the constitutive relations and an expression establishing the temperature evolution is obtained from the first and the second thermodynamics principles. Although most authors carry out this development in the dilated relaxed configuration (Bouvard et al., 2013; Maurel-Pantel et al., 2015), here the process has been developed in the dilated configuration $\overline{\Omega}$ as it is the common intermediate configuration of the two constitutive branches. The local form of balance energy and Clausius-Duhem inequality expressed in the dilated configuration $\overline{\Omega}$ can be obtained as (see Appendix A for more details)

$$\dot{\bar{e}} + \bar{e}\mathrm{tr}\left(\overline{\mathbf{D}}^{\theta}\right) = \overline{\mathbf{M}}_{\mathbf{I}} : \overline{\mathbf{D}}^{\mathbf{p}} + \overline{\mathbf{M}}_{\mathbf{I}} : \overline{\mathbf{D}}^{\theta} + \bar{\mathbf{S}}_{\mathbf{I}} : \mathbf{F}^{\mathbf{MT}}\mathbf{d}_{\mathbf{I}}^{\mathbf{e}}\mathbf{F}^{\mathbf{M}} + \overline{\mathbf{M}}_{\mathbf{N}} : \overline{\mathbf{D}}^{\theta} + \bar{\mathbf{S}}_{\mathbf{N}} : \mathbf{F}^{\mathbf{MT}}\mathbf{d}_{\mathbf{N}}^{\mathbf{e}}\mathbf{F}^{\mathbf{M}} - \overline{\nabla}_{\mathbf{x}}\overline{\mathbf{Q}} + \bar{\mathbf{R}} \tag{15}$$

where $\bar{e}$ is the specific internal energy, $\overline{\mathbf{Q}}$ is the heat flux per unit area and $\bar{\mathbf{R}}$ is the heat source per unit volume in $\overline{\Omega}$. $\bar{\mathbf{S}}_{\mathbf{I}}$ is the second Piola-Kirchhoff stress of the intermolecular resistance expressed in $\overline{\Omega}$ as $\bar{\mathbf{S}}_{\mathbf{I}} = \mathrm{J}^{\mathbf{M}}\mathbf{F}_{\mathbf{I}}^{-\mathbf{M}}\boldsymbol{\sigma}_{\mathbf{I}}\mathbf{F}_{\mathbf{I}}^{-\mathbf{MT}}$ and $\overline{\mathbf{M}}_{\mathbf{I}} = \mathbf{F}_{\mathbf{I}}^{\mathbf{MT}}\mathbf{F}_{\mathbf{I}}^{\mathbf{M}}\bar{\mathbf{S}}_{\mathbf{I}}$ is the Mandel stress in $\overline{\Omega}$. $\bar{\mathbf{S}}_{\mathbf{N}}$ and $\overline{\mathbf{M}}_{\mathbf{N}}$ are the corresponding stress tensors of the network resistance.

$$\dot{\bar{\eta}} + \bar{\eta}\mathrm{tr}\left(\overline{\mathbf{D}}^{\theta}\right) - \frac{\bar{\mathbf{R}}}{\theta} + \frac{1}{\theta}\overline{\nabla}_{\mathbf{x}}\overline{\mathbf{Q}} - \frac{1}{\theta^2}\overline{\mathbf{Q}}\overline{\nabla}_{\mathbf{x}}\theta \geq 0 \tag{16}$$

where $\bar{\eta}$ is the specific internal entropy per unit volume and θ is the current temperature.

The Helmholtz free energy per unit volume in $\overline{\Omega}$, $\bar{\Psi}$, is defined as a function of the internal energy and entropy by

$$\bar{\Psi} = \bar{e} - \theta\bar{\eta} \tag{17}$$

and expressed in rate form

$$\dot{\bar{\Psi}} = \dot{\bar{e}} - \dot{\theta}\bar{\eta} - \theta\dot{\bar{\eta}} \tag{18}$$

The Clausius-Duhem inequality can be alternatively expressed by using Eq. (17) and substituting the expression for $\bar{\mathbf{R}}$ from Eq. (15) into Eq. (16)

$$-\dot{\overline{\Psi}}-\dot{\theta}\overline{\eta}-\overline{\Psi}\mathrm{tr}\left(\overline{\mathbf{D}}^{\theta}\right)+\overline{\mathbf{M}}_{\mathbf{I}}:\overline{\mathbf{D}}^{\mathbf{p}}+\overline{\mathbf{M}}_{\mathbf{I}}:\overline{\mathbf{D}}^{\theta}+\overline{\mathbf{M}}_{\mathbf{N}}:\overline{\mathbf{D}}^{\theta}+\overline{\mathbf{S}}_{\mathbf{I}}:\mathbf{F}^{\mathbf{MT}}\mathbf{d}_{\mathbf{I}}^{\mathbf{e}}\mathbf{F}^{\mathbf{M}}+\overline{\mathbf{S}}_{\mathbf{N}}:\mathbf{F}^{\mathbf{MT}}\mathbf{d}_{\mathbf{N}}^{\mathbf{e}}\mathbf{F}^{\mathbf{M}}-\frac{1}{\theta}\overline{\mathbf{Q}}\overline{\nabla}_{\mathbf{x}}\theta\geq 0 \tag{19}$$

The Helmholtz free energy function was assumed to be the combination of both deformation resistance contributions as $\overline{\Psi}=\overline{\Psi}^{\mathrm{I}}(\mathbf{C}_{\mathbf{I}}^{\mathbf{e}},\theta)+\overline{\Psi}^{\mathrm{N}}(\mathbf{C}_{\mathbf{N}}^{\mathbf{e}})$ (Reese, 1998; Vladimirov et al., 2010; Brepols et al., 2014). These components of the Helmholtz free energy function are directly related to the stress contribution of the Neo-Hookean spring in the case of the intermolecular resistance, $\overline{\Psi}^{\mathrm{I}}(\mathbf{C}_{\mathbf{I}}^{\mathbf{e}},\theta)$, and to the stress contribution of the modification of the 8-chain model in case of the network resistance, $\overline{\Psi}^{\mathrm{N}}(\mathbf{C}_{\mathbf{N}}^{\mathbf{e}})$. Both functions can be found elsewhere (Bergström, 2015; Anand, 1996). Therefore, the Helmholtz free energy function was assumed to depend on the tensors $\mathbf{C}_{\mathbf{I}}^{\mathbf{e}}=\mathbf{F}_{\mathbf{I}}^{\mathbf{eT}}\mathbf{F}_{\mathbf{I}}^{\mathbf{e}}$ and $\mathbf{C}_{\mathbf{N}}^{\mathbf{e}}=\mathbf{F}_{\mathbf{N}}^{\mathbf{eT}}\mathbf{F}_{\mathbf{N}}^{\mathbf{e}}$ and temperature as $\overline{\Psi}=\overline{\Psi}(\mathbf{C}_{\mathbf{I}}^{\mathbf{e}},\mathbf{C}_{\mathbf{N}}^{\mathbf{e}},\theta)$ (see Appendix B for more details). Thus, the rate of $\overline{\Psi}$ can be calculated as

$$\dot{\overline{\Psi}}=\frac{\partial\overline{\Psi}}{\partial\mathbf{C}_{\mathbf{I}}^{\mathbf{e}}}:\dot{\mathbf{C}}_{\mathbf{I}}^{\mathbf{e}}+\frac{\partial\overline{\Psi}}{\partial\mathbf{C}_{\mathbf{N}}^{\mathbf{e}}}:\dot{\mathbf{C}}_{\mathbf{N}}^{\mathbf{e}}+\frac{\partial\overline{\Psi}}{\partial\theta}\dot{\theta} \tag{20}$$

The first terms of the right hand side of Eq. (20) can be written as

$$\begin{aligned}&(\mathrm{a})\frac{\partial\overline{\Psi}}{\partial\mathbf{C}_{\mathbf{I}}^{\mathbf{e}}}:\dot{\mathbf{C}}_{I}^{\mathbf{e}}=\frac{\partial\overline{\Psi}}{\partial\mathbf{C}_{\mathbf{I}}^{\mathbf{e}}}:\left(\dot{\mathbf{F}}_{\mathbf{I}}^{\mathbf{eT}}\mathbf{F}_{\mathbf{I}}^{\mathbf{e}}+\mathbf{F}_{\mathbf{I}}^{\mathbf{eT}}\dot{\mathbf{F}}_{I}^{\mathbf{e}}\right)=2\mathbf{F}_{\mathbf{I}}^{\mathbf{e}}\frac{\partial\overline{\Psi}}{\partial\mathbf{C}_{\mathbf{I}}^{\mathbf{e}}}\mathbf{F}_{\mathbf{I}}^{\mathbf{eT}}:\dot{\mathbf{F}}_{I}^{\mathbf{e}}\mathbf{F}_{\mathbf{I}}^{-\mathbf{e}}=2\frac{\partial\overline{\Psi}}{\partial\mathbf{C}_{\mathbf{I}}^{\mathbf{e}}}:\mathbf{F}_{\mathbf{I}}^{\mathbf{eT}}\mathbf{d}_{\mathbf{I}}^{\mathbf{e}}\mathbf{F}_{\mathbf{I}}^{\mathbf{e}}\\&(\mathrm{b})\frac{\partial\overline{\Psi}}{\partial\mathbf{C}_{\mathbf{N}}^{\mathbf{e}}}:\dot{\mathbf{C}}_{\mathbf{N}}^{\mathbf{e}}=\frac{\partial\overline{\Psi}}{\partial\mathbf{C}_{\mathbf{N}}^{\mathbf{e}}}:\left(\dot{\mathbf{F}}_{\mathbf{N}}^{\mathbf{eT}}\mathbf{F}_{\mathbf{N}}^{\mathbf{e}}+\mathbf{F}_{\mathbf{N}}^{\mathbf{eT}}\dot{\mathbf{F}}_{\mathbf{N}}^{\mathbf{e}}\right)=2\mathbf{F}_{\mathbf{N}}^{\mathbf{e}}\frac{\partial\overline{\Psi}}{\partial\mathbf{C}_{\mathbf{N}}^{\mathbf{e}}}\mathbf{F}_{\mathbf{N}}^{\mathbf{eT}}:\dot{\mathbf{F}}_{\mathbf{N}}^{\mathbf{e}}\mathbf{F}_{\mathbf{N}}^{-\mathbf{e}}=2\frac{\partial\overline{\Psi}}{\partial\mathbf{C}_{\mathbf{N}}^{\mathbf{e}}}:\mathbf{F}_{\mathbf{N}}^{\mathbf{eT}}\mathbf{d}_{\mathbf{N}}^{\mathbf{e}}\mathbf{F}_{\mathbf{N}}^{\mathbf{e}}\end{aligned} \tag{21}$$

Assuming $\mathbf{F}^{\theta}$ isotropic, $\overline{\mathbf{D}}^{\theta}=f_{\theta}\dot{\theta}\mathbf{I}$ can be expressed in terms of a temperature-dependent function f_{θ}, as Bouvard and co-authors proposed (2013), and then $\mathrm{tr}(\overline{\mathbf{D}}^{\theta})=3f_{\theta}\dot{\theta}$. Substituting these terms and Eqs. (20) and (21) in Eq. (19), the Clausius-Duhem inequality can be rewritten as

$$\begin{aligned}&\mathbf{F}_{\mathbf{I}}^{\mathbf{p}}\overline{\mathbf{S}}_{\mathbf{I}}\mathbf{F}_{\mathbf{I}}^{\mathbf{pT}}-2\frac{\partial\overline{\Psi}}{\partial\mathbf{C}_{\mathbf{I}}^{\mathbf{e}}}\Big):\mathbf{F}_{\mathbf{I}}^{\mathbf{eT}}\mathbf{d}_{\mathbf{I}}^{\mathbf{e}}\mathbf{F}_{\mathbf{I}}^{\mathbf{e}}+\quad\overline{\mathbf{S}}_{\mathbf{N}}-2\frac{\partial\overline{\Psi}}{\partial\mathbf{C}_{\mathbf{N}}^{\mathbf{e}}}\Big):\mathbf{F}_{\mathbf{N}}^{\mathbf{eT}}\mathbf{d}_{\mathbf{N}}^{\mathbf{e}}\mathbf{F}_{\mathbf{N}}^{\mathbf{e}}+\overline{\mathbf{M}}_{\mathbf{I}}:\overline{\mathbf{D}}^{\mathbf{p}}+\quad-\frac{\partial\overline{\Psi}}{\partial\theta}-3f_{\theta}\overline{\Psi}-\overline{\eta}+\\&f_{\theta}(\overline{\mathbf{M}}_{\mathbf{I}}+\overline{\mathbf{M}}_{\mathbf{N}}):\mathbf{I}\Big)\dot{\theta}-\frac{1}{\theta}\overline{\mathbf{Q}}\overline{\nabla}_{\mathbf{x}}\theta\geq 0\end{aligned} \tag{22}$$

Following the standard arguments used in the Coleman and Noll method (Coleman and Noll, 1963; Coleman and Gurtin, 1967), Eq. (22) must hold for any arbitrary variation of deformation and temperature. Then, the first, second and fourth terms of this equation must vanish. In this way, the second Piola-Kirchhoff stress associated with each constitutive branch, and the specific internal entropy per unit volume can be written as

$$\overline{\mathbf{S}}_{\mathbf{I}}=\mathbf{F}_{\mathbf{I}}^{-\mathbf{p}}2\frac{\partial\overline{\Psi}}{\partial\mathbf{C}_{\mathbf{I}}^{\mathbf{e}}}\mathbf{F}_{\mathbf{I}}^{-\mathbf{pT}} \tag{23.1}$$

$$\overline{\mathbf{S}}_{\mathbf{N}}=2\frac{\partial\overline{\Psi}}{\partial\mathbf{C}_{\mathbf{N}}^{\mathbf{e}}} \tag{23.2}$$

$$\overline{\eta}=-\frac{\partial\overline{\Psi}}{\partial\theta}-3f_{\theta}\overline{\Psi}+f_{\theta}(\overline{\mathbf{M}}_{\mathbf{I}}+\overline{\mathbf{M}}_{\mathbf{N}}):\mathbf{I} \tag{23.3}$$

Now, it is possible to reduce the dissipation inequality to

$$\overline{\mathbf{M}}_{\mathbf{I}}:\overline{\mathbf{D}}^{\mathbf{p}}-\frac{1}{\theta}\overline{\mathbf{Q}}\overline{\nabla}_{\mathbf{x}}\theta\geq 0 \tag{24}$$

The above equations can be combined to derive the heat equation. The rate of the free energy, Eq. (20), is rewritten now as

$$\dot{\overline{\Psi}}=\frac{1}{2}\mathbf{F}_{\mathbf{I}}^{\mathbf{p}}\overline{\mathbf{S}}_{\mathbf{I}}\mathbf{F}_{\mathbf{I}}^{\mathbf{pT}}:\dot{\mathbf{C}}_{\mathbf{I}}^{\mathbf{e}}+\frac{1}{2}\overline{\mathbf{S}}_{\mathbf{N}}:\dot{\mathbf{C}}_{\mathbf{N}}^{\mathbf{e}}+\left(-\overline{\eta}-3f_{\theta}\overline{\Psi}+f_{\theta}(\overline{\mathbf{M}}_{\mathbf{I}}+\overline{\mathbf{M}}_{\mathbf{N}}):\mathbf{I}\right)\dot{\theta} \tag{25}$$

Using this expression in Eq. (17) with Eq. (15)

$$-\overline{\mathbf{M}}_{\mathbf{I}}:\overline{\mathbf{D}}^{\mathbf{p}}+\theta\dot{\overline{\eta}}+3\overline{\eta}f_{\theta}\dot{\theta}+\overline{\nabla}_{\mathbf{x}}\overline{\mathbf{Q}}-\overline{\mathbf{R}}=0 \tag{26}$$

From Eq. (23) and the expressions for both Mandel stress components, $\overline{\mathbf{M}}_I = \mathbf{F}_I^{pT}\mathbf{C}_I^e\mathbf{F}_I^p\overline{\mathbf{S}}_I$ and $\overline{\mathbf{M}}_N = \mathbf{C}_N^e\overline{\mathbf{S}}_N$, the rate of the entropy $\overline{\eta}$ can be obtained by

$$\dot{\overline{\eta}} = -\left[3f_\theta\frac{\partial\overline{\Psi}}{\partial\mathbf{C}_I^e} + \frac{\partial^2\overline{\Psi}}{\partial\theta\partial\mathbf{C}_I^e} - f_\theta\frac{\partial\left(\mathbf{F}_I^{pT}\mathbf{C}_I^e\mathbf{F}_I^p : \overline{\mathbf{S}}_I\right)}{\partial\mathbf{C}_I^e}\right] : \dot{\mathbf{C}}_I^e - \left[3f_\theta\frac{\partial\overline{\Psi}}{\partial\mathbf{C}_N^e} + \frac{\partial^2\overline{\Psi}}{\partial\theta\partial\mathbf{C}_N^e} - f_\theta\frac{\partial\left(\mathbf{C}_N^e : \overline{\mathbf{S}}_N\right)}{\partial\mathbf{C}_N^e}\right] : \dot{\mathbf{C}}_N^e + \frac{\partial\overline{\eta}}{\partial\theta}\dot{\theta} \tag{27}$$

The heat capacity per unit volume at constant volume $\overline{C} = \frac{\partial\overline{e}}{\partial\theta} = \frac{\partial}{\partial\theta}(\overline{\Psi} + \theta\overline{\eta})$ can be related with the last term of Eq. (27), using the expression obtained in Eq. (23.3) as $\overline{C} = \theta\frac{\partial\overline{\eta}}{\partial\theta} - 3f_\theta\overline{\Psi} + f_\theta(\mathbf{F}_I^{pT}\mathbf{C}_I^e\mathbf{F}_I^p : \overline{\mathbf{S}}_I + \mathbf{C}_N^e : \overline{\mathbf{S}}_N)$. Then, the heat equation is found combining Eqs. (26) and (27) as

$$\begin{aligned}\left(\overline{C} + 3f_\theta\overline{e} - f_\theta\left(\mathbf{F}_I^{pT}\mathbf{C}_I^e\mathbf{F}_I^p : \overline{\mathbf{S}}_I + \mathbf{C}_N^e : \overline{\mathbf{S}}_N\right)\right)\dot{\theta} = \overline{\mathbf{M}}_I : \overline{\mathbf{D}}^p + \theta\left[\frac{3}{2}f_\theta\mathbf{F}_I^p\overline{\mathbf{S}}_I\mathbf{F}_I^{pT} - f_\theta\frac{\partial\left(\mathbf{F}_I^{pT}\mathbf{C}_I^e\mathbf{F}_I^p : \overline{\mathbf{S}}_I\right)}{\partial\mathbf{C}_I^e} + \right.\\ \left.\frac{1}{2}\frac{\partial\left(\mathbf{F}_I^p\overline{\mathbf{S}}_I\mathbf{F}_I^{pT}\right)}{\partial\theta}\right] : \dot{\mathbf{C}}_I^e + \theta\left[\frac{3}{2}f_\theta\overline{\mathbf{S}}_N - f_\theta\frac{\partial\left(\mathbf{C}_N^e : \overline{\mathbf{S}}_N\right)}{\partial\mathbf{C}_N^e} + \frac{1}{2}\frac{\partial\left(\overline{\mathbf{S}}_N\right)}{\partial\theta}\right] : \dot{\mathbf{C}}_N^e - \nabla_x\overline{\mathbf{Q}} + \overline{R}\end{aligned} \tag{28}$$

The first term of the right side in Eq. (28) represents plastic dissipation and the second, third and fourth terms represent the temperature evolution due to thermoelastic coupling. Notice that, in the formulation presented, the total plastic work is assumed to be converted into heat.

2.4. Thermal expansion

The thermal expansion is assumed to be isotropic, being the contribution of the thermal part to the deformation gradient defined in the form

$$\dot{\mathbf{F}}^\theta = f_\theta\mathbf{F}^\theta\dot{\theta} \tag{29}$$

where $\dot{\theta}$ is the time derivative of current temperature and $f_\theta = \alpha_\theta$ is the thermal expansion coefficient.

2.5. Intermolecular resistance: thermoviscoplasticity relations

This part of the model describes a hyperelastic-thermoviscoplastic response due to intermolecular resistance. The second Piola-Kirchhoff stress tensor in $\overline{\overline{\Omega}}$ can be obtained from Eq. (23.1) and the relationship $\overline{\overline{\mathbf{S}}}_I = J_I^{-p}\mathbf{F}_I^p\overline{\mathbf{S}}_I\mathbf{F}_I^{pT}$. This tensor is related to the Cauchy stress tensor by $\boldsymbol{\sigma}_I = J_I^{-e}\mathbf{F}_I^e\overline{\overline{\mathbf{S}}}_I\mathbf{F}_I^{eT}$. Therefore, the contribution of the intermolecular resistance to the Cauchy stress tensor finally reads as

$$\boldsymbol{\sigma}_I = \frac{\lambda_0\ln(J_I^e)}{J_I}\mathbf{I} + \frac{\mu_0}{J_I}(\mathbf{B}_I^e - \mathbf{I}) \tag{30}$$

λ_0 and μ_0 being the classical Lamé constants of the linearized theory depending on the Young's modulus E and the Poisson coefficient ν associated with the linear spring. Young's modulus E usually varies with temperature in semi-crystalline thermoplastic polymers (Rae et al., 2007; Brown et al., 2007). In line with Bouvard et al. (2013), we chose an expression for E(θ) with a linear dependence on temperature, which was observed to fit well with the experimental data

$$E(\theta) = E_{ref} + E_1\left(\theta - \theta_{ref}\right) \tag{31}$$

where E_{ref} is the Young's modulus at the reference temperature θ_{ref} and E_1 is a material parameter. The elastic left Cauchy-Green deformation tensor, $\mathbf{B}_I^e$, can be written as

$$\mathbf{B}_I^e = \mathbf{F}_I^e\mathbf{F}_I^{eT} \tag{32}$$

The yield criterion is written as

$$f_I = \overline{\overline{\sigma}}_{eqI} - \sigma_T = 0 \tag{33}$$

The Rhagava equivalent stress $\overline{\overline{\sigma}}_{eqI}$ has been employed to include the pressure dependency in the yield function (Raghava et al., 1973; Raghava and Caddell, 1973)

$$\bar{\bar{\sigma}}_{eqI} = \frac{(\alpha-1)I_{1I} + \sqrt{(\alpha-1)^2 I_{1I^2} + 12\alpha J_{2I}}}{2\alpha} \tag{34}$$

where α is a material parameter describing the pressure sensitivity and $I_{1I} = \mathrm{tr}\,\bar{\bar{M}}_I$ and $J_{2I} = \frac{1}{2}\bar{\bar{M}}_I^{dev} : \bar{\bar{M}}_I^{dev}$ are stress invariants of the Mandel stress tensor $\bar{\bar{M}}_I = \bar{\bar{C}}_I^e \bar{\bar{S}}_I$ expressed in the configuration $\bar{\bar{\Omega}}$. Polanco-Loria et al. (2010) assume σ_T constant. In this work, a functional dependence on temperature has been defined for σ_T to include the softening in flow stress due to thermal effects as

$$\sigma_T = \sigma_{T0}\left(1 - \left(\frac{\theta - \theta_{ref}}{\theta_{melt} - \theta_{ref}}\right)^m\right) \tag{35}$$

where σ_{T0} is the value of σ_T at reference temperature in uniaxial tension, m is a temperature sensitivity parameter and θ_{melt} is the melting temperature of the material considered. By varying the parameter m, it is possible to control the temperature sensitivity of the material. The expression used in Eq. (35) has been employed in order to define thermal softening in polymers (Louche et al., 2009; Garcia-Gonzalez et al., 2015a) and presents a potential dependence on θ according to the Stefan-Boltzmann theory.

The plastic component of the deformation gradient is defined from the expression which relates the plastic part of the velocity gradient, $\bar{\bar{L}}_I^p$, with the temporal variation of the plastic deformation gradient, $\dot{\bar{\bar{F}}}_I^p$, Eq. (11). In order to define the plastic velocity gradient on the dilated relaxed configuration $\bar{\bar{\Omega}}$, a non-associated viscoplastic flow rule is assumed following the formulation proposed by Polanco-Loria et al. (2010) as

$$\bar{\bar{L}}_I^p = \dot{\bar{\gamma}}_I^p \bar{\bar{r}}_I; \quad \bar{\bar{r}}_I = \frac{\partial g_I}{\partial \bar{\bar{M}}_I} \tag{36}$$

$\dot{\bar{\gamma}}_I^p$ being the viscoplastic multiplier and $\bar{\bar{r}}_I$ the gradient of the plastic potential g_I on $\bar{\bar{\Omega}}$ defined by

$$g_I = \frac{(\beta-1)I_{1I} + \sqrt{(\beta-1)^2 I_{1I^2} + 12\beta J_{2I}}}{2\beta} \tag{37}$$

where β is a parameter which controls the volumetric plastic strain.

The plastic flow direction $\bar{\bar{r}}_I$ on $\bar{\bar{\Omega}}$ is obtained as

$$\bar{\bar{r}}_I = \frac{\partial g_I}{\partial \bar{\bar{M}}_I} = f_1 \mathbf{I} + f_2 \bar{\bar{M}}_I^{dev} \tag{38}$$

where the functions f_1 and f_2 read

$$f_1 = \frac{\partial g_I}{\partial I_{1I}} = \frac{\beta-1}{2\beta} + \frac{(\beta-1)^2 I_{1I}}{2\cdot\beta\sqrt{(\beta-1)^2 I_{1I^2} + 12\beta J_{2I}}} \tag{39}$$

$$f_2 = \frac{\partial g_I}{\partial J_{2I}} = \frac{3}{\sqrt{(\beta-1)^2 I_{1I^2} + 12\beta J_{2I}}} \tag{40}$$

The viscoplastic multiplier $\dot{\bar{\gamma}}_I^p$, depends on the rate-sensitivity parameters $\dot{\varepsilon}_{0I}$ and C, and indirectly on the temperature through σ_T

$$\dot{\bar{\gamma}}_I^p = \begin{cases} 0 & \text{if } f_I \le 0 \\ \dot{\varepsilon}_{0I}\left\{\exp\left[\frac{1}{C}\left(\frac{\bar{\bar{\sigma}}_{eqI}}{\sigma_T} - 1\right)\right] - 1\right\} & \text{if } f_I > 0 \end{cases} \tag{41}$$

2.6. Network resistance

As mentioned earlier, this part of the model describes a hyperelastic entropic resistance originally proposed by Arruda and Boyce (1993). The second Piola-Kirchhoff stress tensor in $\bar{\bar{\Omega}}$ can be obtained from the strain energy potential defined

according to Anand et al. (1996), Eq. (23.2), and it is related by $\boldsymbol{\sigma}_N = J_N^{-1}\mathbf{F}_N\bar{\mathbf{S}}_N\mathbf{F}_N^T$ with the Cauchy stress tensor. Thus, the contribution of this part to the Cauchy stress is defined as

$$\boldsymbol{\sigma}_N = \frac{C_R}{3J_N}\frac{\bar{\lambda}_L}{\bar{\lambda}}\mathfrak{L}^{-1}\left(\frac{\bar{\lambda}}{\bar{\lambda}_L}\right)\left(\mathbf{B}_N^* - \bar{\lambda}^2\mathbf{I}\right) + \frac{\kappa \ln(J_N)\mathbf{I}}{J_N} \tag{42}$$

where $\mathfrak{L}^{-1}$ is the inverse of the Langevin function, CR is the initial elastic modulus of the network resistance, $\bar{\lambda}_L$ is the locking stretch and κ is a bulk modulus. The average total stretch ratio $\bar{\lambda}$ is calculated following Eq. (43)

$$\bar{\lambda} = \sqrt{\frac{1}{3}\mathrm{tr}\left(\mathbf{B}_N^*\right)} \tag{43}$$

The distortional left Cauchy-Green deformation tensor, $\mathbf{B}_N^*$, represents the distortional part of $\mathbf{F}_N^e$ defined by

$$\mathbf{B}_N^* = \mathbf{F}_N^*\left(\mathbf{F}_N^*\right)^T \tag{44}$$

where

$$\mathbf{F}_N^* = J_N^{-1/3}\mathbf{F}_N \tag{45}$$

The contribution of the network resistance to the deformation gradient can be obtained from Eq. (9).

The developed constitutive model has been implemented in the FE code ABAQUS/Explicit to describe the thermomechanical behavior of semi-crystalline thermoplastic polymers. Once the constitutive model is defined, it is necessary to identify the parameters for the material being considered.

3. Identification of model parameters for PEEK polymer

3.1. Baseline material

In this section, the proposed constitutive model is used to deal with the thermomechanical behavior of polyether-ether-ketone (PEEK) of grade 450 G. PEEK is a high-performance semi-crystalline thermoplastic polymer with excellent mechanical and thermal properties as well as good chemical resistance that make it suitable to be used as an engineering material for high-quality applications. Thanks to these chemical and physical properties, PEEK is nowadays regarded as one of the most efficient thermoplastics and it is increasingly employed as matrix material for composites or directly unfilled in biomedical, aeronautic and automotive industries.

PEEK is an ideal candidate to be thermomechanically defined by the proposed constitutive model as its behavior depends on both strain rate and temperature. Regarding temperature sensitivity, the thermal history has a fundamental influence on its mechanical properties, e.g. yield stress, impact resistance, fracture toughness, etc., since these are highly dependent on the crystalline morphology and degree of crystallinity (Rae et al., 2007, Garcia-Gonzalez et al., 2015a). Another interesting aspect of PEEK is that adiabatic heating associated with dynamic processes can induce rapid crystallization on reaching high temperature increments (Hamdan and Swallowe, 1996). In this regard, temperature tracking upon the deformation process is quite important since this polymer presents some relaxation temperatures which vary with strain rate (Jordan et al., 2007). The glass transition of the amorphous phase is found at 422 K, the melting temperature of the crystalline phase at 616 K and the beta transition temperature, related with a ductile-to-brittle transition (Adams and Gaitonde, 1993; Garcia-Gonzalez et al., 2015a), at around 213 K in quasi-static conditions. Furthermore, its Young's modulus presents dependence with temperature decreasing as temperature increases (Díez-Pascual et al., 2012).

3.2. Identification process

The identification process to obtain the model parameters for semi-crystalline thermoplastic polymers is based on the correspondence of the parameters with the mechanical response of the material in terms of the following blocks:

(i) *Linear response*: the model parameters E_{ref}, E_1 and ν are related to the elastic contribution to the intermolecular resistance and determine the initial elastic response of the material depending on temperature. E_{ref} and E_1 define the initial slopes of the stress-strain curves depending on temperature and ν is the Poisson ratio.

(ii) *Yield stress*: the parameters σ_{T0}, C, $\dot{\varepsilon}_{0A}$ and m define the yield stress of the material. C and $\dot{\varepsilon}_{0A}$ are associated with the nonlinear viscoplastic dashpot of the intermolecular resistance and σ_{T0} and m with the friction element of the intermolecular resistance which defines the yield function. C and $\dot{\varepsilon}_{0A}$ determine the strain rate sensitivity of yield stress and m the temperature sensitivity.

(iii) *Network response*: the network contribution to the stress state is established by the parameters C_R, $\overline{\lambda}_L$ and κ. Both parameters C_R and $\overline{\lambda}_L$ are associated with the spring element of network resistance. C_R is related to the initial elastic modulus of network resistance. The parameter $\overline{\lambda}_L$ is related to the maximum (fully extended) stretch that a molecule can be exposed to and κ is a bulk modulus used in applications where the mechanical behavior of the material is only defined by the network contribution (e.g. rubber modeling).

(iv) *Volumetric plastic strain sensitivity*: the parameter β, which defines the plastic potential, must be identified in order to control inelastic volume change.

(v) *Stress state sensitivity*: the parameter α must be identified to define the pressure sensitivity of the yield stress.

The parameter calibration of the semi-crystalline thermoplastic polymer considered in this study, PEEK, is based on reported mechanical characterization covering a wide range of temperatures and strain rates (Rae et al., 2007). Therefore, knowing the influence of the parameters on the mechanical response of the material in terms of linear response, yielding, network response, volumetric plastic strain and stress state, the identification procedure carried out is presented next.

The parameters E_{ref}, E_1, ν, C, $\dot{\varepsilon}_{0A}$, m, β and α can be directly obtained from the analysis of experimental data, values depicted in Table 1. From uniaxial stress-strain curves at the reference strain rate and for the range of temperatures selected, the model parameters E_{ref} and E_1 are identified in order to define the initial slope of the curves depending on temperature. The Poisson ratio (ν) is determined from the initial relation between transverse and longitudinal strains.

Using the nominal stress-strain curves at different strain rates and temperatures in compression, the parameters C and m are obtained. The strain rate sensitivity parameter C can be found by its relationship with the slope of the yield stress-strain rate curve. The temperature sensitivity parameter m is determined by its relationship with the slope of the yield stress-temperature curve. The reference strain rate $\dot{\varepsilon}_{0A}$ is taken as the lowest strain rate used in compression tests for which experimental data varying the initial temperature are available.

Based on the observations reported by El-Qoubaa and Othman (2014) in regard to the volume change of PEEK over a wide range of strain rates and temperatures, parameter β controlling the volumetric plastic strain has been defined as $\beta = 1$ assuming volume preserving since they showed that PEEK's (visco)-plastic deformation is isochoric, independently of temperature and strain rate. Finally, the parameter α was obtained from the relation observed between the yield stresses reached in uniaxial compression and tensile tests.

A numerical model with the dimensions of the specimens employed in uniaxial compression tests by Rae et al. (2007), defined with C3D8R elements, was developed in ABAQUS/Explicit. This numerical model was used to identify the parameters σ_{T0}, C_R and $\overline{\lambda}_L$ from the true stress-strain curves shown in Fig. 3a as the main targets in comparing the experimental and predicted curves.

In these numerical simulations, temperature evolution has been included considering uniquely specific energy due to inelastic dissipation and heat conduction. Thermoelastic coupling is neglected in line with published studies for thermoplastic polymers (Bouvard et al., 2013). Therefore, the temperature evolution can be obtained from Eq. (28) as:

$$\dot{\theta} = \frac{\overline{\mathbf{M}_\mathbf{I}} : \overline{\mathbf{D}^\mathbf{p}}}{\overline{C}} - \frac{\overline{\nabla_x}\overline{\mathbf{Q}}}{\overline{C}} \tag{46}$$

Regarding the numerical implementation of the heat equation, the term associated to plastic dissipation was defined by updating the inelastic energy dissipated in each time increment. Moreover, the heat conduction is solved by the standard equation implemented in Abaqus considering the temperature as an extra degree of freedom.

Following the procedure proposed by Kendall and coauthors (2013; 2014) using equation (47), the rate at which the system is expected to behave adiabatically has been approximated from the size of the specimen, μ_t, and the thermal diffusivity of the specimen material, δ.

$$\delta = k/\rho\overline{C} \tag{47.1}$$

Table 1
Material parameters for PEEK.

Initial elastic properties					Intermolecular resistance					
E_{ref} (GPa)	E_1 (MPa)	ν	$\dot{\varepsilon}_{0A}$ (s^{-1})	C	σ_{T0} (MPa)	m	θ_{ref} (K)	θ_{melt} (K)	α	β
3.2	−3.0	0.4	0.001	0.038	108	0.69	296	616	1.2	1.0
General properties					Network resistance					
ρ (kg/m^3)		$\overline{C}$ (kJ/m^3K)		α_θ (K^{-1})	C_R (MPa)		$\overline{\lambda}_L$		κ	
1300		2834		$4.6\text{-}10^{-6}$	0.4		5.5		0.0	

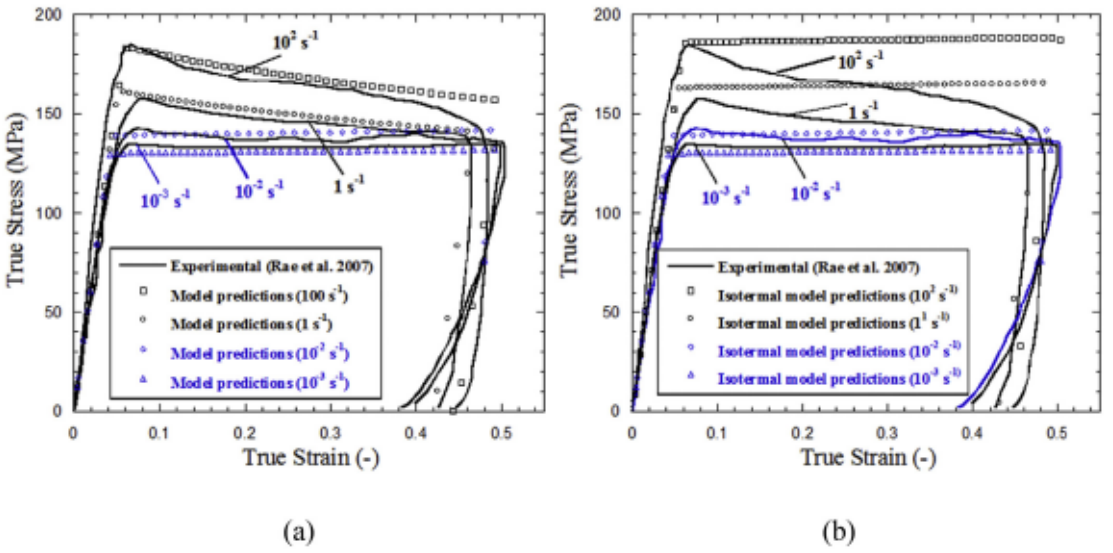

Fig. 3. Stress-strain experimental curves of PEEK at room temperature for different strain rate (Rae et al., 2007) versus: (a) model predictions; (b) predictions with isothermal hypothesis.

$$\mu_t = 2\sqrt{\delta\tau} \tag{47.2}$$

$$\dot{\varepsilon} = 1/\tau \tag{47.3}$$

k being the thermal conductivity and τ a characteristic timescale for thermal diffusion. For PEEK compression specimens, the values of ρ and $\overline{C}$ are shown in Table 1, k = 0.32 W/mK and $\mu_t = 6.375$ mm. Solving Eq. (47), a characteristic strain rate was found at $\dot{\varepsilon} \approx 10^{-2}\ s^{-1}$. This characteristic strain rate is assumed as a reference value at which adiabatic heating is expected (Kendall and Siviour, 2013; Kendall and Siviour, 2014), and in such conditions thermal flow is neglected. Additionally, at strain rates lower than the characteristic one, isothermal conditions were assumed which permit to neglect the term associated to the inelastic dissipation. The parameters which finally define the PEEK material behavior are depicted in Table 1.

Good agreement between the model predictions and experimental data (Rae et al., 2007) was found in terms of Young's Modulus, stress-strain curves, Fig. 3a, and in terms of yield stress depending on pressure, strain rate and temperature sensitivities, Figs. 4 and 5. It can be observed in Fig. 3b that, if isothermal conditions are assumed, the model predictions are considerably worse than the ones obtained for adiabatic conditions for strain rates higher than $\dot{\varepsilon} \approx 10^{-2}\ s^{-1}$, Fig. 3a. Moreover,

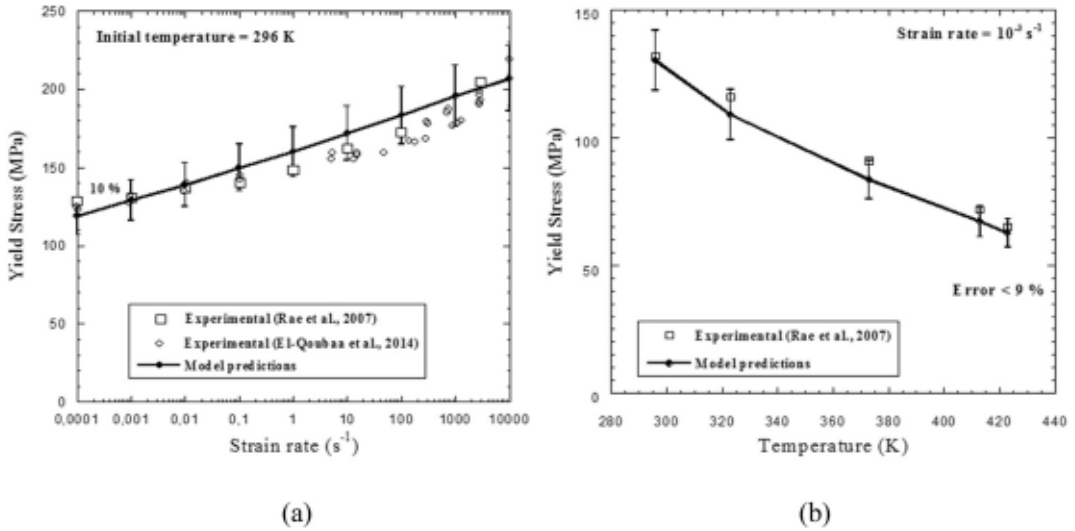

Fig. 4. Experimental data (Rae et al., 2007; El-Qoubaa,2014) versus model predictions in terms of: (a) strain rate sensitity; and (b) temperature sensitivity of PEEK for uniaxial compression tests.

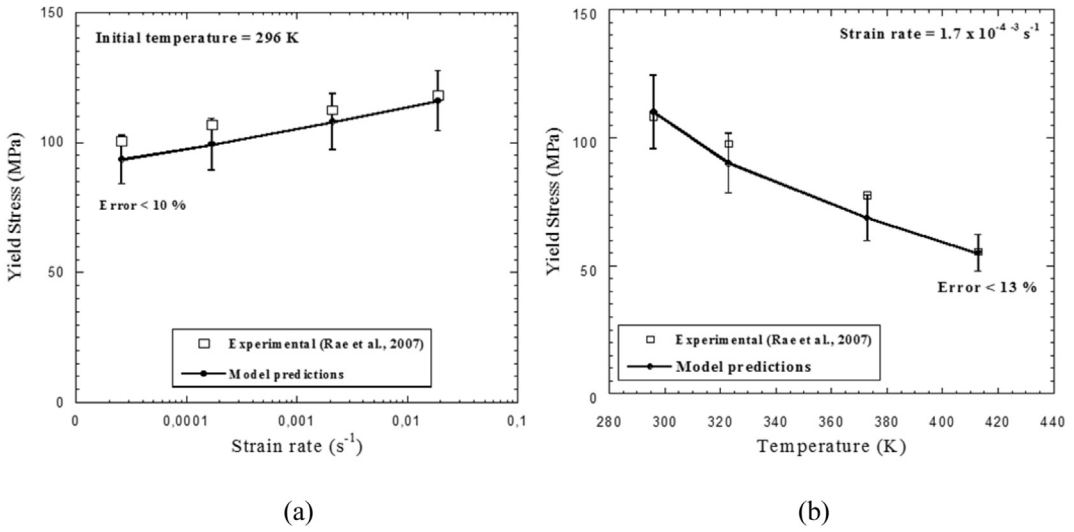

Fig. 5. Experimental data (Rae et al., 2007) versus model predictions of: (a) strain rate sensitity; and (b) temperature sensitivity of PEEK for uniaxial tensile tests.

as it can be seen in Figs. 4(b) and 5(b), the predictive capacity of the model is limited by the glass transition temperature. Around this value and thereafter, the degree of crystallinity and also the specific heat are no more constants for semi-crystalline polymer (Santos et al., 2013).

According to previous observations, the consideration of temperature evolution due to plastic dissipation and its associated material softening has been found to play an essential role. Aiming to highlight this effect, a finite element model has been developed in order to observe the importance of considering temperature evolution due to plastic dissipation, its associated material softening and its coupling with strain rate. These considerations are essential to achieve a good definition of the material response. The model is defined by a single element on which tension-compression cycles reaching considerable plastic strains are applied under adiabatic conditions imposing a displacement varying with time, Fig. 6a. This configuration allows us to isolate the contribution of the inelastic dissipation term in the heat equation, permitting the study of the coupling between strain rate and inelastic dissipation and the subsequent thermal softening induced. The model predictions for the evolution of yield stresses reached as the temperature increases due to plastic dissipation during the tension-compression cycles are showed in Fig. 6b. This loading history allows us to achieve significant temperature increments and continuous thermal softening without reaching failure strain, Fig. 6b.

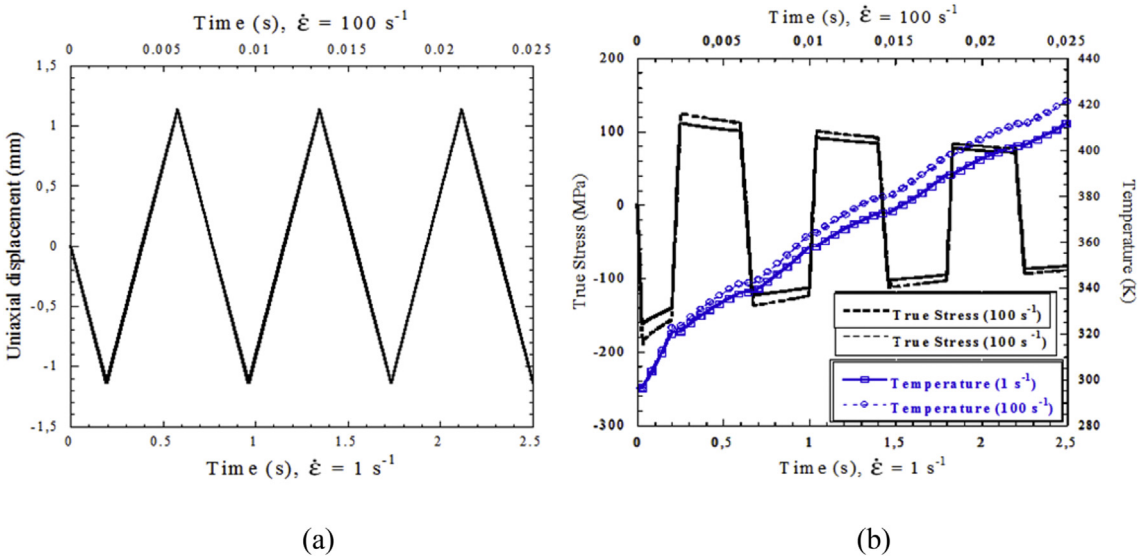

Fig. 6. (a) Applied displacement history in the tension-compression cycles; (b) Stress-time and temperature-time curve for tension-compression cycles.

During the first cycle the compressive behavior follows the same path observed in a single test, Fig. 3a. Moreover, the evolution of stress and temperature for the following cycles brings forth relevant observations:

- The compressive pre-strain modifies the subsequent tensile stress-strain behavior, and introduces a strain-induced anisotropy via network resistance, as can be noticed from the different values of tension and compression yield stresses, Fig. 6b. The stress induced by the spring of the network response then acts as a backstress with respect to the intermolecular response as Polanco-Loria et al. (2010) observed.
- A continuous increase in temperature, Fig. 6b, activated just as the material undergoes plastic dissipation. For the tension-compression cycles imposed, the temperature evolves considerably, implying a continuous softening in the material behavior. A strong coupling between strain rate and temperature evolution due to plastic dissipation is observed, leading to higher temperature increments with higher strain rates. Material hardening associated with strain rate increases the stress level reached at higher strain rates, resulting in higher values of plastic dissipation and increases in temperature.

4. Influence of thermal effects in dynamic deformation processes of semi-crystalline polymers

In this section, the importance of taking into account thermal effects on the semi-crystalline polymers behavior is underlined. This consideration becomes more significant under dynamic loading conditions where there is a strong coupling between strain rate and thermal effects. Therefore, two different dynamic problems are presented: (i) Low velocity impact test on thin plates and (ii) dynamic necking on slender bar.

4.1. Low velocity impact test on PEEK thin plates

This section details the study and results of impact testing on PEEK plates. This problem was selected because impact loadings involve large and irreversible deformations, high strain rates and temperature increment due to plastic dissipation. The analysis considers impact energy (controling both impact velocity and striker mass), evolution of the impact force versus striker displacement and testing temperature.

4.1.1. Experimental set-up

A drop weight tower was used to conduct the impact tests, providing a perpendicular impact on the unfilled PEEK plates. This configuration allows control of both the impact velocity and the mass of the impactor in order to achieve the required impact energy. Two testing configurations of 11.25 J and 125 J were selected for the experiments. The first configuration involves a mass and an impact velocity equal to 3.6 kg and 2.5 m/s respectively, and the second configuration involves a mass and an impact velocity equal to 10 kg and 5 m/s respectively. The lower energy was found to induce appreciable inelastic deformation and the higher energy was found to be close to the perforation limit. In addition, a climatic chamber was employed, allowing variations in the initial testing temperature (θ_o) from 293 K to 373 K.

Square specimens with an area equal to $A_t = 130 \times 130\ mm^2$ and a thickness of 3 mm were used. They were clamped by using screws around a circular active area 100 mm in diameter (Fig. 7a). In order to avoid any perturbation during the test, the

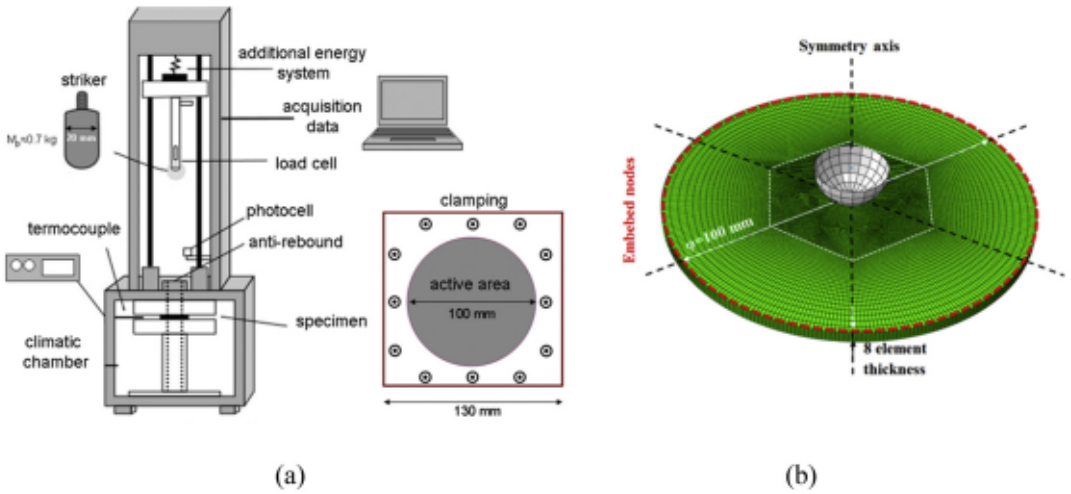

Fig. 7. (a) Experimental set-up for impact test; and (b) mesh of the numerical model for impact test.

screws were symmetrically fixed. The mass of the steel striker is $M_p = 0.70$ kg with a hemispherical nose of 20 mm diameter. The effective mass (M_{total}) was varied from 3.6 kg until 10 kg by adding aditional mass to the setup.

A local cell placed on the striker provides its time dependent displacement $\delta_s(t)$ during the impact process, by integration of the impact force versus time curve F(t)

$$\delta_s(t) = \int_0^t \left[V_o \int_0^\tau \frac{F(\xi) - M_{total} g}{M_{total}} d\xi \right] d\tau \tag{48}$$

where g is the gravity acceleration.

After the impact and if no perforation of the plate occurred, the striker is hold by an anti-rebound system in order to avoid multi-hits on the specimen.

4.1.2. Definition of the numerical model

The experimental tests were simulated with a Lagrangian 3D finite element model developed in ABAQUS/Explicit (Abaqus v6.12 analysis user's manual, 2012). The geometry of the plate was selected to be representative of the active area of the experimental test specimens (100 mm in diameter) with a thickness of 3 mm. Fig. 7b shows the target mesh, where eight elements were distributed across the thickness of the plate. This is in consonance with the reccomendations reported elsewhere (Abaqus v6.12 analysis user's manual, 2012), where it is suggested that, when modeling any structure carrying bending loads, at least four elements should be employed through the thickness. The type of elements used to define the mesh was tri-linear elements with reduced integration (C3D8R in ABAQUS notation). The impact zone presents a mesh refinement composed of 90,000 elements. In order to reduce the computational time, the peripherical zone was meshed with 64,800 elements increasing progressively the element size until reaching the perimeter of the target. A convergence study was carried out using different mesh densities until an optimum configuration was obtained. Moreover, the numerical analysis carried out satisfies the energy balance accounting for kinetic energy, external forces and internal forces (considering both elastic and inelastic components). Regarding the modelization of the striker, it has been defined as a rigid body since the experimental observations revealed absence of plastic deformation or erosion on its surface after the impact. The contact striker/plate was defined by a constant friction coefficient $\mu = 0.2$ (Borruto, 2010). The constant value employed for this coefficient is based on the assumption of a approximately constant pressure along the striker-plate contact zone confirmed by FE analysis of different projectile-target configurations (Wang and Shi, 2013). For the maximum energy simulation at which perforation is reached, a failure criterion based on a constant deformation equal to $\bar{\varepsilon}^f_{total} = 1.2$ was assumed consistently with failure values reported by Sobieraj et al. (2009) and Garcia-Gonzalez and coauthors (2015).

4.1.3. Results and analysis

The numerical results provided by the constitutive model presented have been compared with experimental data. The force-displacement curves from the experimental tests and numerical simulations are shown in Fig. 8 depending on impact energy, Fig. 8a, and testing temperature, Fig. 8b. A good correlation was found between experimental and numerical results, with a maximum error lower than 10% in terms of maximum force reached and the corresponding displacement to maximum load, which demonstrates that the model used in this study faithfully reproduces the behavior of the PEEK polymer under low velocity impact test. The shape of the force-displacement curve is fairly well captured in both loading and unloading branches. The numerical model predicts the decrease observed in the slope of experimental force-displacement curves due to thermal softening as the initial testing temperature is increased. The model also reproduces the increase in the maximum peak of force reached depending on the impact energy and the strain rate imposed in each test. Moreover, the thermal softening is not only due to the initial testing temperature but also due to the temperature evolution induced by plastic dissipation. This effect can be observed in Fig. 9, which shows isothermal and adiabatic estimations, resulting in a much better prediction for situations in which adiabatic heating effects and thermal softening are considered. This fact could explain the overestimation of the maximum peak of force reached by other authors (Polanco-Loria et al., 2010) who do not consider temperature increment due to plastic dissipation and the consequent softening.

The consideration of thermal effects is essential to know if the glass transition temperature is reached. It also provides a good prediction of the softening induced in the specimen which determines the slope of the force-displacement curve and the maximum peak of force reached. For all the experimental tests conducted, the final temperature reached after the impact was numerically predicted. These results show that the glass transition is not exceeded, so it can be concluded that the numerical predictions are valid and no sudden change in the material behavior occurs. Moreover, Fig. 10 compares, in terms of force-displacement curves, the model predictions for the previous test of Fig. 9, and when a higher initial temperature (373 K) is imposed. The difference in terms of thermal softening between both initial temperature conditions is remarkable. It can be observed that even if the initial temperature is lower than the glass transition temperature, this last one is reached upon the deformation process due to plastic dissipation. Therefore, the temperature prediction allows for evaluating if the material is working between the ductile-to-brittle and the glass transition temperatures.

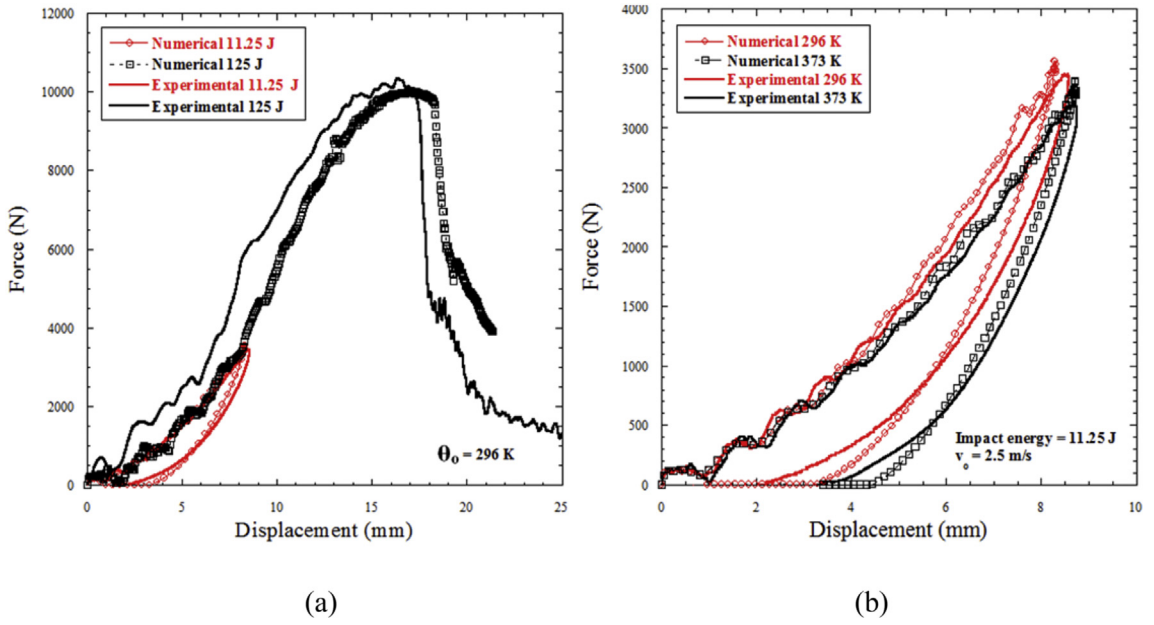

Fig. 8. Numerical and experimental force-displacement curves for low velocity impact tests: (a) different impact energy; (b) different initial testing temperatures.

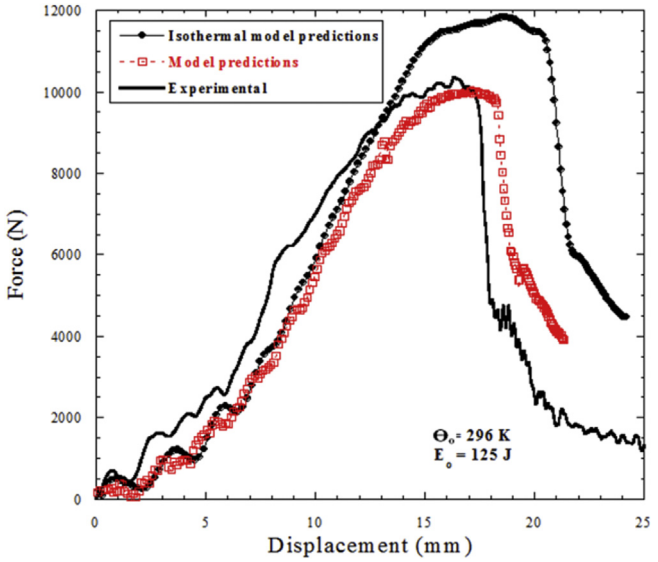

Fig. 9. Model predictions and experimental force-displacement curves for impact tests: influence of considering plastic dissipation effects in model versus isothermal conditions.

4.2. Dynamic necking in a PEEK slender bar

Necking is an early indication of failure and, therefore, it is commonly utilized as a reference for evaluating the energy absorption capacity (Rodríguez-Martínez et al., 2013a). The term necking strain denotes the stage at which full concentration of plastic flow in the neck region occurs and there is a surrounding zone where plastic flow can be neglected.

Once the predictions of the constitutive model shown a good correlation with experimental data under dynamic conditions, a parametric study has been developed in order to analyze the inertial and thermal effects on the necking and energy absorption capacity of thermoplastic semi-crystalline polymers (PEEK) by simulating cylindrical slender bars subjected to dynamic stretching. While this problem has been widely studied in metal materials, it has not been thoroughly investigated in semi-crystalline polymers. The numerical model presented below provides the localized necking strain $\bar{\varepsilon}_{neck}$ and specific

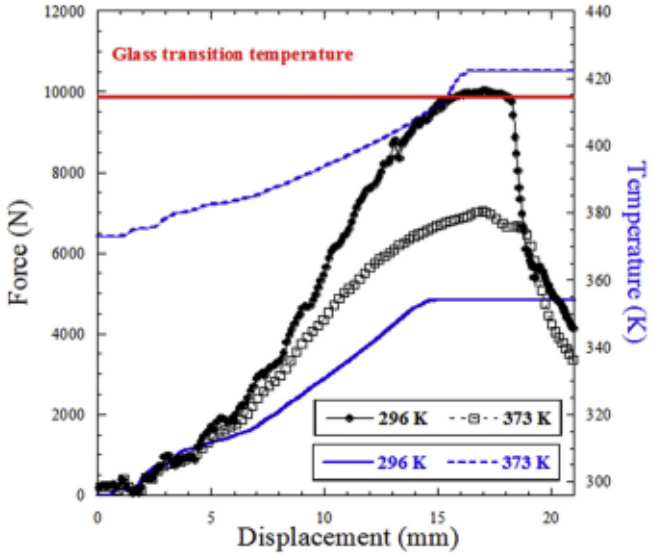

Fig. 10. Numerical force-displacement curves and temperature evolution for impact test at kinetic impact energy equal to 125 J and initial testing temperatures equal to 296 K and 373 K.

energy absorbed until neck inception, E_{neck}. These variables are good indicators of the material ductility and energy absorption capacity, respectively. The localized necking strain, hereafter referred to as necking strain, has been determined in the numerical computations following the procedure reported elsewhere (Triantafyllidis and Waldenmyer, 2004; Xue et al., 2008; Zaera et al., 2014). The necking event is assumed to be determined by the condition $d\overline{\varepsilon}^p/dt = 0$, where $\overline{\varepsilon}^p$ is the equivalent plastic strain, evaluated within the zone which surrounds the neck,

$$\overline{\varepsilon}^p = \int_0^t \dot{\overline{\varepsilon}}^p d\tau \tag{49}$$

where $\dot{\overline{\varepsilon}}^p$ is the plastic strain rate defined as

$$\dot{\overline{\varepsilon}}^p = \sqrt{\frac{2}{3}\overline{\mathbf{D}}_I^p : \overline{\mathbf{D}}_I^p} \tag{50}$$

Under these conditions, the necking strain is defined as the total longitudinal strain,

$$\overline{\varepsilon}_{neck} = \ln\left(\frac{L}{L_o}\right) \tag{51}$$

where L is the current bar length and L_o the initial one.

It must be noticed that no damage criterion is defined for these simulations. The specific energy absorbed per unit volume until neck inception, is defined by the relationship

$$E_{neck} = \frac{\int_o^{u_{neck}} F du}{V_o} \tag{52}$$

where V_o is the initial volume of the cylindrical bar, F is the current force applied on the specimen, u is the longitudinal displacement of the end $z=L_o$ and u_{neck} is the displacement at localized necking.

4.2.1. Definition of the numerical model

A cylindrical slender bar with an initial length $L_o = 2\cdot10^{-2}$ m and a circular cross section radius $r_o = 5\cdot10^{-4}$ m has been studied. A constant stretching velocity is applied on one side of the bar. The movement of the opposite side is restricted in the axial direction. The imposed loading conditions can be formulated as $V_z(r,L_o,t) = \dot{\varepsilon}_o L_o$ and $V_z(r,0,t) = 0$, where t is the time and $\dot{\varepsilon}_o$ the initial strain rate. Following the methodology proposed by Zaera et al. (2014), specific initial conditions consistent with the boundary conditions have been imposed in order to avoid the propagation of waves along the bar caused by the application of these boundary conditions in a solid at rest. Then, the initial axial velocity field is defined following the expression

$V_z(r,z,0) = \dot{\varepsilon}_o\, z$, where z is the coordinate along the axis. The initialization of V_z was found sufficient to avoid wave propagation, without including the initialization of stress state and radial velocity. In addition, an initial temperature is imposed on the whole specimen which evolves or not depending on the thermal assumptions taken into account in the test.

The presented problem was modeled with the Lagrangian 3D FE code ABAQUS/Explicit (Abaqus v6.12 analysis user's manual, 2012). The mesh of the model has been defined involving 3200 tri-linear elements with reduced integration (C3D8R in ABAQUS notation). The numerical round-off was sufficient to perturb the stress and the strain fields. Therefore, both geometrical and material imperfections were not introduced into the model (Rusinek and Zaera, 2007; Vadillo et al., 2012). Moreover, the energy balance has been verified for the numerical simulations.

4.2.2. Results and analysis

The results and analysis of this section are focused on the following aspects: inertia, thermal softening and thermo-mechanical coupling. The term inertia plays a stabilizing role contributing to delay necking formation and can be defined as

$$I = \frac{r_o^2\, \dot{\bar{\varepsilon}}^2\, \rho}{\sigma_o} \tag{53}$$

r_o being a characteristic dimension and σ_o the yield stress. In a dimensionless form of the equation of movement for the problem formulation of dynamically stretching 1D solids, I is the inertial factor multiplying the acceleration. Strain rate and material hardening influence necking inception and energy absorption capacity of the material. Actually, inertia plays the main role in the material stabilization at high deformation rates, being it dominant over the hardening effects (Rodríguez-Martínez et al., 2013b). To focus exclusively on the effect of inertia, temperature evolution due to plastic dissipation and thermal flow were not taken into account assuming isothermal conditions, Fig. 11. This figure shows necking strain depending on initial strain rate at a reference temperature equal to 296 K. A monotonic and non-linear increase in the necking strain with loading rate is observed in accordance with Eq. (53) since inertia contributes to delay necking formation. The specific energy absorbed, as it occurs with necking strain, increases continuously and non-linearly whith the loading rate. This behavior finds agreement with evidences reported for metallic materials (Altynova et al., 1996; Rodríguez-Martinez et al., 2013).

Initial temperature influences necking inception and energy absorption capacity of the material. Now focusing on the influence of initial temperature, isothermal conditions were considered allowing us to develop a parametric study depending on this variable, Fig. 12. This figure presents necking strain and specific energy depending on initial temperature at a reference strain rate equal to 10^4 s^{-1} under isothermal conditions. An increase in necking strain and a decrease in specific energy absorbed with temperature is observed. The first tendency is due to the decrease of yield stress with temperature which, according to Eq. (53), produces a stabilizing effect through inertia. However, this decrease in ductility does not translate into a decrease in specific energy absorption. This fact can be explained by the reduction in flow stress, Fig. 3, which is found to be dominant over the gain in ductility.

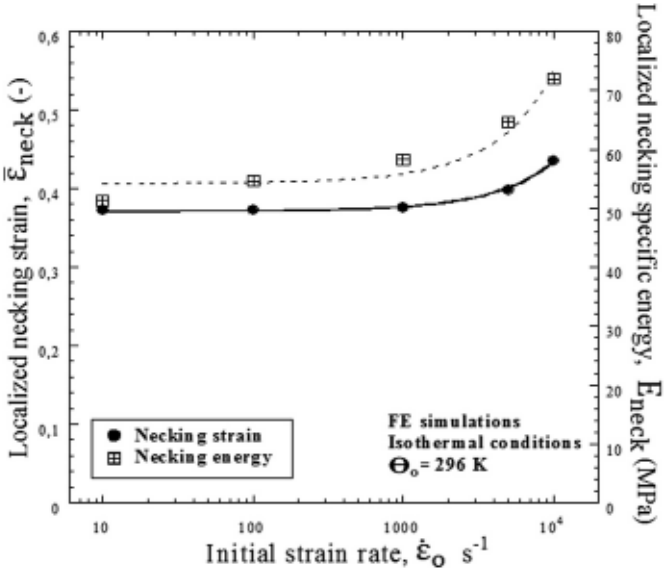

Fig. 11. Localized necking strain and necking specific energy versus loading strain rate for PEEK polymer assuming isothermal conditions.

In order to consider coupled thermomechanical effects, Fig. 13 presents the comparison between the results for isothermal and adiabatic conditions. This figure shows the effect of temperature evolution upon the deformation process leading to material softening in combination with material hardening due to strain rate effects. The importance of taking into account the plastic dissipation is shown in terms of necking strain and specific energy absorbed. In this regard, Fig. 14 shows the strain, temperature and plastic strain rate contours of the deformed specimen for adiabatic conditions. This figure allows for visualizing the localization of the plastic strain rate in the necking zone and the consequent increase of temperature due to inelastic effects.

Under isothermal conditions, numerical results showed a similar tendency of both necking strain and specific energy absorbed with strain rate, as well as under adiabatic conditions, Fig. 13a–b. Regarding thermal effects, the predictions obtained under isothermal conditions may mistakenly suggest that necking strain must be greater under adiabatic conditions due to the temperature evolution since necking strain increases with initial testing temperature. However, under adiabatic conditions, there is a competition between the stabilizing role played by the decrease in yield stress due to temperature

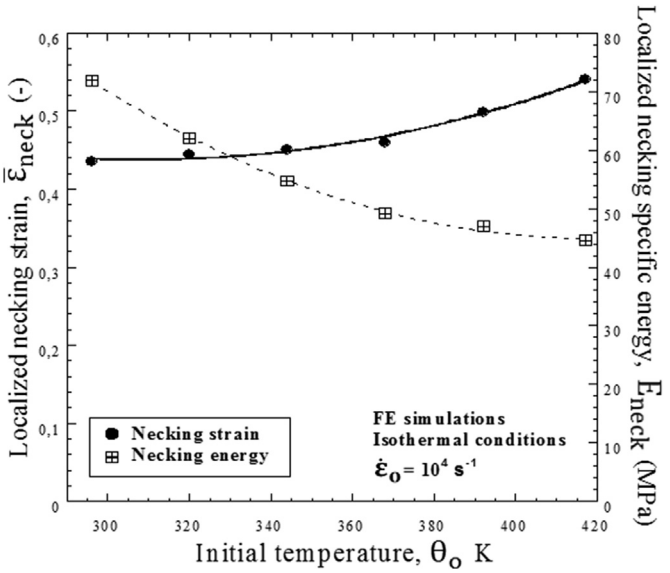

Fig. 12. Localized necking strain and necking specific energy versus initial temperature for PEEK assuming isothermal conditions.

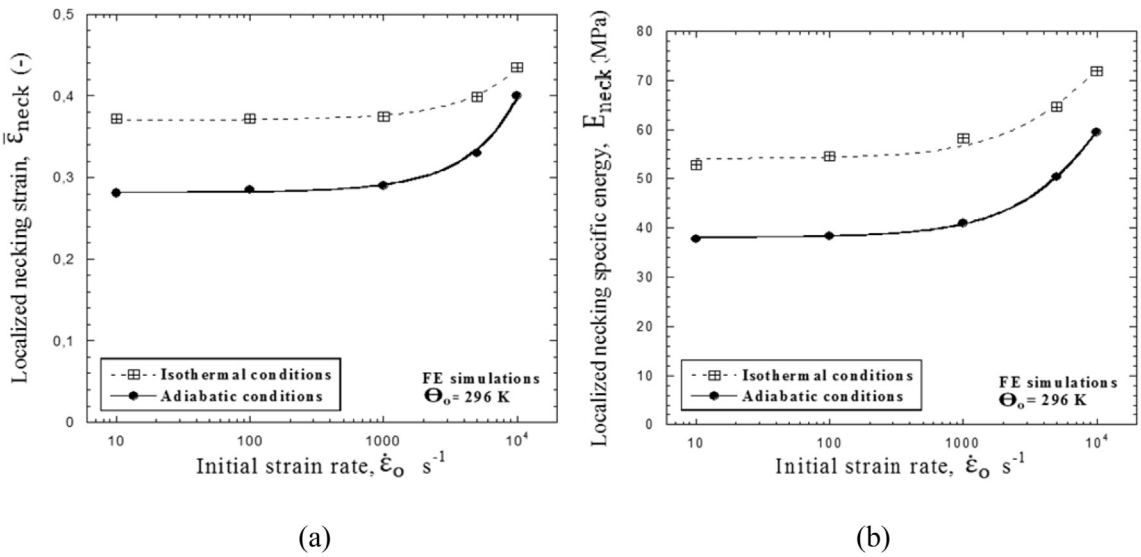

Fig. 13. (a) Localized necking strain versus loading strain rate for PEEK; (b) Specific energy per unit volume versus loading strain rate for PEEK assuming temperature evolution due to plastic dissipation.

increase and the destabilizing role played by thermal softening from that point. Some studies have shown that larger necking strains are reached as the material hardening is more significant (Chalal and Abed-Meraim, 2015; Rodríguez-Martínez et al., 2015). In this regard, as can be observed in Fig. 3 for strain rates higher than $\dot{\varepsilon} \approx 10^{-2}$, while PEEK behaves in a perfectly plastic way under isothermal conditions, it presents a negative hardening due to thermal softening induced by plastic dissipation. This fact leads to higher necking strains when plastic dissipation is not considered. In the higher rate regime, the results show that inertia governs the onset of the localization being dominant over material softening. Regarding absorbed specific energy, it is much lower when plastic dissipation is taken into account because of the lower values of force reached due to thermal softening. Therefore, despite the dominant role of inertia, temperature evolution must be considered in order to achieve more realistic results in terms of ductility and energy absorption capacity.

5. Concluding remarks

The main contributions of this work are the following:

- A thermomechanical constitutive model for semi-crystalline polymers has been developed accounting for strain rate and temperature. Moreover, a consistent thermodynamic framework has been established for the model.
- The constitutive model has been implemented in a FE code and its parameters have been identified for PEEK polymer from experimental data from available literature covering a wide range of strain rates and temperatures for both tension and compression states. Good agreement between numerical predictions and experimental data was found in terms of stress-strain curves depending on strain rate and temperature. For high strain rates, the consideration of temperature evolution and thermal softening plays an essential role to obtain accurate predictions. Aiming to highlight these thermal effects, additional numerical simulations of tension-compression cycles have been carried out. A strong coupling between strain rate and temperature evolution due to plastic dissipation was found, leading to higher temperature increments and material softening with higher strain rates.
- The predictive capacity of the model has been evaluated in two different dynamic problems: **i)** low velocity impact tests on PEEK thin plates and **ii)** dynamic necking on PEEK slender bar.

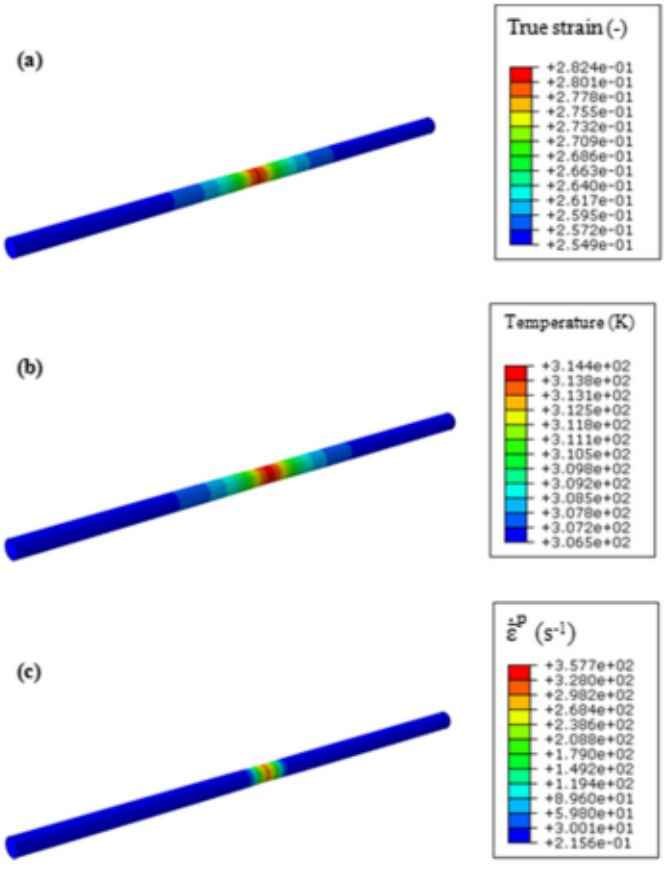

Fig. 14. (a) True strain, (b) temperature and (c) plastic strain rate contours of the deformed specimen at necking event under adiabatic conditions at 10 s^{-1}.

i) Good agreement between numerical predictions and experimental data was found in terms of force-displacement curves depending on impact energy and initial testing temperature. Better predictions were found when softening associated to plastic dissipation is taken into account, which determines the slope of the force-displacement curve and the peak force reached. In addition, the numerical prediction of temperature evolution is essential to determine if the glass transition temperature is reached.

ii) A numerical parametric study of the inertial and thermal effects on the ductility and energy absorption capacity of PEEK was carried out for isothermal and adiabatic conditions. Under isothermal conditions, a clear dependence of both necking strain and specific energy absorbed on strain rate was found. Increasing initial temperature and strain rate leads to increasing necking strain and decreasing energy absorption. For adiabatic conditions, despite the dominant role of inertia, plastic dissipation must be taken into account in order to achieve more realistic results in terms of ductility and energy absorption capacity and not overestimate them. In this regard, both necking strain and specific energy absorbed were found to decrease when plastic dissipation is considered in comparison with isothermal conditions.

The results presented in this paper demonstrate the capacity of the model proposed to predict the thermomechanical behavior of semi-crystalline polymers and the importance of taking into account the coupling between strain rate and temperature effects.

Acknowledgements

The researchers are indebted to the Ministerio de Economía y Competitividad de España (Project DPI2014-57989-P) for the financial support which permitted to conduct part of this work. The authors express their thanks to Ms. Penelope Miller, Mr. Sergio Puerta, Mr. David Pedroche for their technical support.

Appendix A. Description of Eqs. (15) and (16)

According to Holzapfel (2000), the reduced global form of energy balance expressed in spatial description is taken as the starting point

$$\frac{D}{Dt}\int_{\Omega} e dv = \int_{\Omega} (\boldsymbol{\sigma} : \mathbf{d} - \nabla_x \mathbf{q} + r) dv \tag{A.1}$$

e being the specific internal energy per unit volume, $\mathbf{q}$ the heat flux per unit area and r the heat source per unit volume in Ω. The left hand side term of this equation can be rewritten by taking into account the relation between elemental volumes in $\Omega(dv)$, $\overline{\Omega}(d\overline{V})$ and $\Omega_0(dV)$, namely $dv = J^M d\overline{V} = J dV$, then:

$$\frac{D}{Dt}\int_{\Omega} e dv = \frac{D}{Dt}\int_{\Omega_0} e_o dV = \int_{\overline{\Omega}} \left(\dot{\overline{e}} + \overline{e} tr\left(\overline{\mathbf{D}}^{\theta}\right)\right) d\overline{V} \tag{A.2}$$

where e_0 is the specific internal energy per unit volume in Ω_0, and the relation $\frac{\partial J^*}{\partial t} = J^{\theta} tr(\overline{\mathbf{D}}^{\theta})$ has been used. Notice that since the reference volume V is independent of time, the previous expression can be written $\frac{D}{Dt}\int_{\Omega_0} e_0 dV = \int_{\Omega_0} \dot{e}_0 dV$.

The right hand term in Eq. (A.1), can be written in the different configurations as

$$\int_{\Omega} (\boldsymbol{\sigma} : \mathbf{d} - \nabla_x \mathbf{q} + r) dv = \int_{\Omega_0} \left(\mathbf{P} : \dot{\mathbf{F}} - \nabla_X \mathbf{Q} + R\right) dV = \int_{\overline{\Omega}} (\boldsymbol{\sigma} : \mathbf{d} - \nabla_x \mathbf{q} + r) J^M d\overline{V} \tag{A.3}$$

where $\mathbf{P}$, $\mathbf{Q}$ and R respectively are the first Piola-Kirchhoff stress, the heat flux per unit area and the heat source per unit volume in Ω_0.

The stress power per unit volume in Ω can be expressed using Eqs. (10) and (13) and considering the definition of the velocity gradient $\mathbf{l} = \mathbf{d} + \mathbf{w}$, as

$$\boldsymbol{\sigma} : \mathbf{d} = \boldsymbol{\sigma} : (\mathbf{l} - \mathbf{w}) = \boldsymbol{\sigma} : \mathbf{l} - \boldsymbol{\sigma} : \mathbf{w} = \boldsymbol{\sigma} : \mathbf{l} = \boldsymbol{\sigma}_{\mathbf{I}} : \mathbf{l} + \boldsymbol{\sigma}_{\mathbf{N}} : \mathbf{l} \tag{A.4}$$

where $\mathbf{d}$ is the total rate of deformation tensor and $\mathbf{w}$ is the total spin tensor.

Using the velocity gradient decomposition, Eq. (10), it is possible to develop the term associated with the intermolecular contribution to the stress per unit volume as

$$\boldsymbol{\sigma}_I : \mathbf{l} = \boldsymbol{\sigma}_I : \mathbf{l}_I^e + \boldsymbol{\sigma}_I : \mathbf{F}_I^e \overline{\overline{\mathbf{L}}}_I^p \mathbf{F}_I^{-e} + \boldsymbol{\sigma}_I : \mathbf{F}_I^e \mathbf{F}_I^p \overline{\mathbf{L}}^\theta \mathbf{F}_I^{-p} \mathbf{F}_I^{-e} = \boldsymbol{\sigma}_I : \mathbf{d}_I^e + \boldsymbol{\sigma}_I : \mathbf{F}_I^e \overline{\overline{\mathbf{D}}}_I^p \mathbf{F}_I^{-e} + \boldsymbol{\sigma}_I : \mathbf{F}^M \overline{\mathbf{D}}^\theta \mathbf{F}^{-M} \tag{A.5}$$

Rearranging this equation and expressing it in the dilated configuration $\overline{\Omega}$

$$\boldsymbol{\sigma}_I : \mathbf{l} = J^{-M}\left(\overline{\mathbf{M}}_I : \overline{\mathbf{D}}^p + \overline{\mathbf{M}}_I : \overline{\mathbf{D}}^\theta + \overline{\mathbf{S}}_I : \mathbf{F}^{MT} \mathbf{d}_I^e \mathbf{F}^M\right) \tag{A.6}$$

Using the velocity gradient decomposition, Eq. (12), it is possible to develop the term associated with the network contribution to the stress per unit volume as

$$\boldsymbol{\sigma}_N : \mathbf{l} = \boldsymbol{\sigma}_N : \mathbf{l}_N^e + \boldsymbol{\sigma}_N : \mathbf{F}_N^e \overline{\mathbf{L}^\theta} \mathbf{F}_N^{-e} = \boldsymbol{\sigma}_N : \mathbf{d}_N^e + \boldsymbol{\sigma}_N : \mathbf{F}_N^e \overline{\mathbf{D}^\theta} \mathbf{F}_N^{-e} \tag{A.7}$$

Rearranging this equation and expressing it in the dilated configuration $\overline{\Omega}$

$$\boldsymbol{\sigma}_N : \mathbf{l} = J^{-M}\left(\overline{\mathbf{M}}_N : \overline{\mathbf{D}}^\theta + \overline{\mathbf{S}}_N : \mathbf{F}^{MT} \mathbf{d}_N^e \mathbf{F}^M\right) \tag{A.8}$$

Using the expressions developed in Eqs. (A.2), (A.3), (A.6) and (A.8) into Eq. (A.1), the local form of the balance energy can be expressed in the dilated configuration $\overline{\Omega}$ as

$$\dot{\overline{e}} + \overline{e}\,\mathrm{tr}\left(\overline{\mathbf{D}}^\theta\right) = \overline{\mathbf{M}}_I : \overline{\mathbf{D}}^p + \overline{\mathbf{M}}_I : \overline{\mathbf{D}}^\theta + \overline{\mathbf{S}}_I : \mathbf{F}^{MT} \mathbf{d}_I^e \mathbf{F}^M + \overline{\mathbf{M}}_N : \overline{\mathbf{D}}^\theta + \overline{\mathbf{S}}_N : \mathbf{F}^{MT} \mathbf{d}_N^e \mathbf{F}^M - \overline{\nabla}_x \overline{\mathbf{Q}} + \overline{R} \tag{A.10}$$

The global form of the Clausius-Duhem inequality, in spatial description (Holzapfel, 2000) is given by

$$\frac{D}{Dt}\int_\Omega \eta dv + \int_\Omega \left(\nabla_x\left(\frac{\mathbf{q}}{\theta}\right) - \frac{r}{\theta}\right) dv \geq 0 \tag{A.11}$$

This equation can be also written in local form expressed as

$$\dot{\overline{\eta}} + \overline{\eta}\,\mathrm{tr}\left(\overline{\mathbf{D}}^\theta\right) - \frac{\overline{R}}{\theta} + \frac{1}{\theta}\overline{\nabla}_x \overline{\mathbf{Q}} - \frac{1}{\theta^2}\overline{\mathbf{Q}}\overline{\nabla}_x \theta \geq 0 \tag{A.12}$$

Appendix B. Helmholtz free energy

The explicit expression for the Helmholtz free energy $\overline{\Psi} = \overline{\Psi}^I(\mathbf{C}_I^e, \theta) + \overline{\Psi}^N(\mathbf{C}_N^e)$ is presented and the constitutive expressions of the model are derived from it.

The contribution of the intermolecular resistance to the free energy can be defined through the following Neo-Hookean potential energy function (Bergström, 2015):

$$\overline{\Psi}^I(\mathbf{C}_I^e, \theta) = \frac{1}{2}\lambda_0(\theta)\ln(J_I^e) - \mu_0(\theta)\ln(J_I^e) + \frac{1}{2}\mu_0(\theta)\left[\mathrm{tr}(\mathbf{C}_I^e) - 3\right] \tag{B.1}$$

Regarding the contribution of the network resistance to the free energy, it can be defined by potential energy function proposed by Anand (1996):

$$\overline{\Psi}^N(\mathbf{C}_N^e) = C_R \overline{\lambda}_L^2 \left\{ \frac{\overline{\lambda}}{\overline{\lambda}_L}\mathfrak{L}^{-1}\left(\frac{\overline{\lambda}}{\overline{\lambda}_L}\right) + \ln\left[\frac{\mathfrak{L}^{-1}\left(\frac{\overline{\lambda}}{\overline{\lambda}_L}\right)}{\sinh\left[\mathfrak{L}^{-1}\left(\frac{\overline{\lambda}}{\overline{\lambda}_L}\right)\right]}\right]\right\} + \frac{1}{2}\kappa(\ln(J_N))^2 \tag{B.2}$$

The terms $\frac{\partial \overline{\Psi}}{\partial \mathbf{C}_I^e}$, $\frac{\partial \overline{\Psi}}{\partial \mathbf{C}_N^e}$ and $\frac{\partial \overline{\Psi}}{\partial \theta}$ read as

$$\frac{\partial \overline{\Psi}}{\partial \mathbf{C}_I^e} = \frac{1}{2}\lambda_0(\theta)\ln(J_I^e)\mathbf{C}_I^{-e} - \frac{1}{2}\mu_0(\theta)\mathbf{C}_I^{-e} + \frac{1}{2}\mu_0(\theta)\mathbf{I} \tag{B.3}$$

$$\frac{\partial\overline{\Psi}}{\partial\mathbf{C}_{\mathbf{N}}^{\mathbf{e}}}=\frac{1}{2}\frac{C_R}{3}\frac{\bar{\lambda}_L}{\bar{\lambda}}\mathfrak{L}^{-1}\left(\frac{\bar{\lambda}}{\bar{\lambda}_L}\right)\left(\mathbf{I}-\bar{\lambda}^{-2}\mathbf{C}_{\mathbf{N}}^{-1}\right)+\frac{1}{2}\kappa\ln(J_N)\mathbf{C}_{\mathbf{N}}^{-1} \tag{B.4}$$

$$\frac{\partial\overline{\Psi}}{\partial\theta}=\frac{1}{2}\frac{E_1\nu}{(1+\nu)(1-2\nu)}\ln(J_1^e)-\frac{E_1}{2(1+\nu)}\ln(J_1^e)+\frac{1}{2}\frac{E_1}{2(1+\nu)}\left[\mathrm{tr}(\mathbf{C}_1^e)-3\right] \tag{B.5}$$

Therefore, the constitutive equations for both resistances can be derived by using the stress tensors relations $\boldsymbol{\sigma}_I=J_I^{-1}\mathbf{F}_I^{M}\bar{\mathbf{S}}_I\mathbf{F}_I^{MT}$ $\boldsymbol{\sigma}_N=J_N^{-1}\mathbf{F}_N^{M}\bar{\mathbf{S}}_N\mathbf{F}_N^{MT}$ and the equations $\bar{\mathbf{S}}_I=\mathbf{F}_I^{-p}2\frac{\partial\overline{\Psi}}{\partial\mathbf{C}_I}\mathbf{F}_I^{-pT}$ and $\bar{\mathbf{S}}_N=2\frac{\partial\overline{\Psi}}{\partial\mathbf{C}_N}$. Regarding the specific internal entropy per unit volume, it can be derived by using Eq. (B.5) into the following expression

$$\overline{\eta}=-\frac{\partial\overline{\Psi}}{\partial\theta}-3f_\theta\overline{\Psi}+f_\theta\left(\overline{\mathbf{M}}_{\mathbf{I}}+\overline{\mathbf{M}}_{\mathbf{N}}\right):\mathbf{I} \tag{B.6}$$

Appendix C. Time-integration of plastic and thermal flows

The plastic deformation gradient of the intermolecular constitutive branch is obtained by integrating the plastic flow rule, Eq. (11), following the procedure proposed by van Dommelen et al. (2003). The plastic component of the velocity gradient $\overline{\mathbf{L}}_{\mathbf{I}}^{\mathbf{p}}$ is assumed to be constant during each time increment. Thus, the plastic deformation gradient at time level $t_{n+1}=t+\Delta t$ reads as

$$\mathbf{F}_{\mathbf{I}\,\mathbf{n+1}}^{\mathbf{p}}=\mathbf{F}_{\mathbf{I}\,\mathbf{n}}^{\mathbf{p}}\exp\left(\Delta t\overline{\mathbf{L}}_{\mathbf{I}\,\mathbf{n}}^{\mathbf{p}}\right) \tag{C.1}$$

The tensor exponential can be numerically evaluated by the diagonalization of $\overline{\mathbf{L}}_{\mathbf{I}\,\mathbf{n}}^{\mathbf{p}}$ or by the Padé approximation. If Padé approximation is chosen, the incremental plastic deformation gradient reads as

$$\mathbf{F}_{\mathbf{I}\,\mathbf{inc}}^{\mathbf{p}}=\exp\left(\Delta t\,\overline{\mathbf{L}}_{\mathbf{I}\,\mathbf{n}}^{\mathbf{p}}\right)\approx\left(\mathbf{I}-\frac{\Delta t}{2}\overline{\mathbf{L}}_{\mathbf{I}\,\mathbf{n}}^{\mathbf{p}}\right)^{-1}\left(\mathbf{I}+\frac{\Delta t}{2}\overline{\mathbf{L}}_{\mathbf{I}\,\mathbf{n}}^{\mathbf{p}}\right) \tag{C.2}$$

The determinant of the exponential approximation term must be corrected by a straightforward normalization for finite increments because it may deviate from unity:

$$\mathbf{F}_{\mathbf{I}\,\mathbf{n+1}}^{\mathbf{p}}=\left(J_{I\,inc}^{p}\right)^{-1/3}\mathbf{F}_{\mathbf{I}\,\mathbf{inc}}^{\mathbf{p}}\mathbf{F}_{\mathbf{I}\,\mathbf{n}}^{\mathbf{p}} \tag{C.3}$$

being $J_{I\,inc}^{p}=\det(\mathbf{F}_{\mathbf{I}\,\mathbf{inc}}^{\mathbf{p}})$.

Regarding the thermal deformation gradient, it can be obtained by integrating Eq. (29):

$$\mathbf{F}_{\mathbf{n+1}}^{\boldsymbol{\theta}}=\mathbf{F}_{\mathbf{n}}^{\boldsymbol{\theta}}\exp[f_\theta(\theta_{n+1}-\theta_n)] \tag{C.4}$$

In this equation, the current temperature at the end of the increment, θ_{n+1}, can be obtained from Eq. (29) as

$$\theta_{n+1}=\theta_n+\frac{\Delta t}{\left(\overline{C}+3f_\theta\bar{e}_n-f_\theta\left(\mathbf{F}_{\mathbf{I}\,\mathbf{n}}^{\mathbf{pT}}\mathbf{C}_{\mathbf{I}\,\mathbf{n}}^{\mathbf{e}}\mathbf{F}_{\mathbf{I}\,\mathbf{n}}^{\mathbf{p}}:\bar{\mathbf{S}}_{\mathbf{I}\,\mathbf{n}}+\mathbf{C}_{\mathbf{N}\,\mathbf{n}}^{\mathbf{e}}:\bar{\mathbf{S}}_{\mathbf{N}\,\mathbf{n}}\right)\right)}F_n \tag{C.5}$$

where F_n is the sum of the terms associated to inelastic dissipation, thermoelastic coupling, heat conduction and heat sources, Eq. (C.6), evaluated at the beginning of the increment.

$$\begin{aligned}F=\overline{\mathbf{M}}_{\mathbf{I}}:\overline{\mathbf{D}}^{\mathbf{p}}+\theta\Bigg[&\frac{3}{2}f_\theta\mathbf{F}_{\mathbf{I}}^{\mathbf{p}}\bar{\mathbf{S}}_{\mathbf{I}}\mathbf{F}_{\mathbf{I}}^{\mathbf{pT}}-f_\theta\frac{\partial\left(\mathbf{F}_{\mathbf{I}}^{\mathbf{pT}}\mathbf{C}_{\mathbf{I}}^{\mathbf{e}}\mathbf{F}_{\mathbf{I}}^{\mathbf{p}}:\bar{\mathbf{S}}_{\mathbf{I}}\right)}{\partial\mathbf{C}_{\mathbf{I}}^{\mathbf{e}}}+\frac{1}{2}\frac{\partial\left(\mathbf{F}_{\mathbf{I}}^{\mathbf{p}}\bar{\mathbf{S}}_{\mathbf{I}}\mathbf{F}_{\mathbf{I}}^{\mathbf{pT}}\right)}{\partial\theta}\Bigg]:\dot{\mathbf{C}}_I^e+\theta\Bigg[\frac{3}{2}f_\theta\bar{\mathbf{S}}_{\mathbf{N}}-f_\theta\frac{\partial\left(\mathbf{C}_{\mathbf{N}}^{\mathbf{e}}:\bar{\mathbf{S}}_{\mathbf{N}}\right)}{\partial\mathbf{C}_{\mathbf{N}}^{\mathbf{e}}}+\\&\frac{1}{2}\frac{\partial\left(\bar{\mathbf{S}}_{\mathbf{N}}\right)}{\partial\theta}\Bigg]:\dot{\mathbf{C}}_N^e-\nabla_x\overline{\mathbf{Q}}+\overline{\mathbf{R}}\end{aligned} \tag{C.6}$$

References

Adams, R.D., Gaitonde, J.M., 1993. Low-temperature flexural dynamic measurements on PEEK, HTA and some of their carbon fibre composites. Compos. Sci. Technol. 47, 271–287.

Altynova, M., Hu, X., Daehn, G.S., 1996. Increased ductility in high velocity electromagnetic ring expansion. Metall. Trans. A 27, 1837–1844.

Anand, L., 1996. A constitutive model for compressible elastomeric solids. Comput. Mech. 18, 339–355.

Arruda, E.M., Boyce, M.C., 1993. A three-dimensional constitutive model for the large stretch behavior of rubber elastic materials. J. Mech. Phys. Solids 41, 389–412.

Ayoub, G., Zaïri, F., Naït-Abdelaziz, M., Gloaguen, J.M., 2010. Modelling large deformation behaviour under loading–unloading of semicrystalline polymers: application to a high density polyethylene. Int. J. Plast. 26, 329–347.

Bergström, J., 2015. Mechanics of Solid Polymers: theory and computational modeling, first ed. William Andrew, San Diego, USA.

Bergström, J.S., Rimnac, C.M., Kurtz, S.M., 2003. Prediction of multiaxial mechanical behavior for conventional and highly crosslinked UHMWPE using a hybrid constitutive model. Biomaterials 24, 1365–1380.

Billon, N., 2012. New constitutive modelling for time-dependent mechanical behaviour of polymers close to glass transition: fundamental and experimental validation. J. Appl. Polym. Sci. 125 (6), 4390–4401.

Borruto, A., 2010. A new material for hip prosthesis without considerable debris release. Med. Eng. Phys. 32, 908–913.

Bouvard, J.L., Francis, D.K., Tschopp, M.A., Marin, E.B., Bammann, D.J., Horstemeyer, M.F., 2013. An internal state variable material model for predicting the time, thermomechanical, and stress state dependence of amorphous glassy polymers under large deformation. Int. J. Plast. 42, 168–193.

Boyce, M.C., Arruda, E.M., 2000. Constitutive models of rubber elasticity: a review. Rubber Chem. Technol. 73, 504–523.

Boyce, M.C., Parks, D.M., Argon, A.S., 1988. Large inelastic deformation of glassy polymers. part I: rate dependent constitutive model. Mech. Mater. 7, 15–33.

Boyce, M.C., Socrate, S., Llana, P.G., 2000. Constitutive model for the finite deformation stress–strain behavior of poly(ethylene terephthalate) above the glass transition. Polymer 41, 2183–2201.

Brepols, T., Vladimirov, I.N., Reese, S., 2014. Numerical comparison of isotropic hypo- and hyperelastic-based plasticity models with application to industrial forming processes. Int. J. Plast. 63, 18–48.

Brown, E.N., Willms, R.B., Gray, G.T., Rae, P.J., Cady, C.M., Vecchio, K.S., Flowers, J., Martinez, M.Y., 2007. Influence of molecular conformation on the constitutive response of polyethylene: a comparison of HDPE, EHMWPE, and PEX. Exp. Mech. 47, 381–393.

Chalal, H., Abed-Meraim, F., 2015. Hardening effects on strain localization predictions in porous ductile materials using the bifurcation approach. Mech. Mater. 91, 152–166.

Chen, J., Liu, L., Liu, Y., Leng, J., 2014. Thermoviscoelastic shape memory behavior for epoxy-shape memory polymer. Smart Mater. Struct. 23, 055025.

Colak, O.U., Dusunceli, N., 2006. Modeling viscoelastic and viscoplastic behavior of high density polyethylene (HDPE). J. Eng. Mater. T. 128, 572–578.

Coleman, B.D., Gurtin, M.E., 1967. Thermodynamics with internal state variables. J. Chem. Phys. 47, 597.

Coleman, B.D., Noll, W., 1963. The thermodynamics of elastic materials with heat conduction and viscosity. Arch. Ration. Mech. Anal. 13, 167–178.

Dassault Systèmes Abaqus v6.12 Documentation, 2012. ABAQUS Analysis User's Manual. Abaqus Inc.

Díez-Pascual, A.M., Guan, J., Simard, B., Gómez-Fatou, M.A., 2012. Poly(phenylene sulphide) and poly(ether ether ketone) composites reinforced with single-walled carbon nanotube buckypaper: II – mechanical properties, electrical and thermal conductivity. Compos. Part. A. 43, 1007–1015.

Edwards, S.F., Vilgis, Th, 1986. The effect of entanglements in rubber elasticity. Polymer 27, 483–492.

El-Qoubaa, Z., Othman, R., 2014a. Characterization and modeling of the strain rate sensitivity of polyetheretherketone's compressive yield stress. Mater. Des. 66, 336–345.

El-Qoubaa, Z., Othman, R., 2014b. Volume change in PEEK under compression loads over wide ranges of strain rate and temperature. J. Strain Anal. Eng. Des. 49, 315–324.

El-Qoubaa, Z., Othman, R., 2016. Strain rate sensitivity of polyetheretherketone's compressive yield stress at low and high temperatures. Mech. Mater. 95, 15–27.

Garcia-Gonzalez, D., Rodriguez-Millan, M., Rusinek, A., Arias, A., 2015a. Low temperature effect on impact energy absorption capability of PEEK composites. Compos. Struct. 134, 440–449.

Garcia-Gonzalez, D., Rodriguez-Millan, M., Vaz-Romero, A., Arias, A., 2015b. High impact velocity on multi-layered composite of polyether-ether-ketone and aluminium. Compos. Interfaces 8, 705–715.

Garcia-Gonzalez, D., Rusinek, A., Jankowiak, T., Arias, A., 2015c. Mechanical impact behavior of polyether–ether–ketone (PEEK). Compos. Struct. 124, 88–99.

Gaymans, R., Hamber, M., Inberg, J., 2000. The brittle–ductile transition temperature of polycarbonate as function of test speed. Polym. Eng. Sci. 40, 256–262.

Ge, Q., Luo, X., Iversen, C.B., Nejad, H.B., Mather, P.T., Dunn, M.L., Qi, H.J., 2014. A finite deformation thermomechanical constitutive model for triple shape polymeric composites based on dual thermal transitions. Int. J. Solids Struct. 51, 2777–2790.

Gurtin, M.E., Anand, L., 2005. The decomposition F = FeFp, material symmetry, and plastic irrotationality for solids that are isotropic-viscoplastic or amorphous. Int. J. Plast. 21, 1686–1719.

Halabi, F., Rodríguez, J., Rebolledo, L., Hurtos, E., Doblaré, M., 2011. Mechanical characterization and numerical simulation of polyether–ether–ketone (PEEK) cranial implants. J. Mech. Behav. Biomed. 4, 1819–1832.

Hamdan, S., Swallowe, G., 1996. Crystallinity in PEEK and PEK after mechanical testing and its dependence on strain rate and temperature. J. Polym. Sci. Pol. Phys. 34, 699–705.

Haward, R.N., Thackray, G., 1968. The use of a mathematical model to describe isothermal stress-strain curves in glassy thermoplastics. Proc. R. Soc. Lond. Ser. A, Math.Phys. Sci. 302, 453–472.

Holzapfel, G.A., 2000. Nonlinear Solid Mechanics: a Continuum Approach for Engineering. Wiley, Chichester.

Jordan, J.L., Siviour, C.R., Foley, J.R., Brown, E.N., 2007. Compressive properties of extruded polytetrafluoroethylene. Polymer 48, 4184–4195.

Kamlah, M., Tsakmakis, C., 1999. Use of isotropic thermoelasticity laws in ®nite viscoplasticity models. Contin. Mech. Thermodyn. 11, 73–88.

Kendall, M.J., Siviour, C.R., 2013. Experimentally simulating adiabatic conditions: approximating high rate polymer behavior using low rate experiments with temperature profiles. Polymer 54, 5058–5063.

Kendall, M.J., Siviour, C.R., 2014. Novel temperature measurement method & thermodynamic investigations of amorphous polymers during high rate deformation. Polymer 55, 2514–2522.

Krairi, A., Doghri, I., 2014. A thermodynamically-based constitutive model for thermoplastic polymers coupling viscoelasticity, viscoplasticity and ductile damage. Int. J. Plast. 60, 163–181.

Kroner, E., 1960. Allgemeine kontinuumstheorie der versetzungen und eigenspannungen. Arch. Ration. Mech. An. 4, 273–334.

Lee, E., 1969. Elastic-plastic deformation at finite strains. ASME T. J. Appl.Mech. 36.

Li, G., Xu, W., 2011. Thermomechanical behavior of thermoset shape memory polymer programmed by cold-compression: testing and constitutive modeling. J. Mech. Phys. Solids 59, 1231–1250.

Lion, A., 2000. Constitutive modelling in finite thermoviscoplasticity: a physical approach based on nonlinear rheological models. Int. J. Plast. 16, 469–494.

Louche, H., Piette-Coudol, F., Arrieux, R., Issartel, J., 2009. An experimental and modeling study of the thermomechanical behavior of an ABS polymer structural component during an impact test. Int. J. Impact Eng. 36, 847–861.

Maurel-Pantel, A., Baquet, E., Bikard, J., Bouvard, J.L., Billon, N., 2015. A thermo-mechanical large deformation constitutive model for polymers based on material network description: application to a semi-crystalline polyamide 66. Int. J. Plast. 67, 102–126.

Mohagheghian, I., McShane, G.J., Stronge, W.J., 2015. Impact perforation of monolithic polyethylene plates: projectile nose shape dependence. Int. J. Impact Eng. 80, 162–176.

Mulliken, A.D., Boyce, M.C., 2006. Mechanics of the rate-dependent elastic-plastic deformation of glassy polymers from low to high strain rates. Int. J. Solids Struct. 44, 1331–1356.
Nasraoui, M., Forquin, P., Siad, L., Rusinek, A., 2012. Influence of strain rate, temperature and adiabatic heating on the mechanical behaviour of poly-methyl-methacrylate: experimental and modelling analyses. Mater. Des. 37, 500–509.
Polanco-Loria, M., Clausen, A.H., Berstad, T., Hopperstad, O.S., 2010. Constitutive model for thermoplastics with structural applications. Int. J. Impact Eng. 37, 1207–1219.
Popelar, C.F., Popelar, C.H., Kenner, V.H., 2004. Viscoelastic material characterization and modelling of polyethylene. Polym. Eng. Sci. 30, 577–586.
Rae, P., Brown, E., Orler, E., 2007. The mechanical properties of poly(ether-ether-ketone) (PEEK) with emphasis on the large compressive strain response. Polymer 48, 598–615.
Raghava, R., Caddell, R.M., Yeh, G.S.Y., 1973. The macroscopic yield behaviour of polymers. J. Mater. Sci. 8, 225–232.
Raghava, R.S., Caddell, R.M., 1973. Macroscopic yield criterion for crystalline polymers. Int. J. Mech. Sci. 15, 967–974.
Reese, S., 1998. Multiplicative thermo-viscoplasticity: a thermodynamic model and its finite element implementation. Tech. Mech. 18, 209–216.
Rodríguez-Martínez, J.A., Rittel, D., Zaera, R., Osovski, S., 2013a. Finite element analysis of AISI 304 steel sheets subjected to dynamic tension: the effects of martensitic transformation and plastic strain development on flow localization. Int. J. Impact Eng. 53, 206–216.
Rodríguez-Martínez, J.A., Vadillo, G., Fernández-Sáez, J., Molinari, A., 2013b. Identification of the critical wavelength responsible for the fragmentation of ductile rings expanding at very high strain rates. J. Mech. Phys. Solids 61, 1357–1376.
Rodríguez-Martínez, J.A., Vadillo, G., Zaera, R., Fernández-Sáez, J., Rittel, D., 2015. An analysis of microstructural and thermal softening effects in dynamic necking. Mech. Mater. 80, 298–310.
Rusinek, A., Zaera, R., 2007. Finite element simulation of steel ring fragmentation under radial expansión. Int. J. Impact Eng. 34, 799–822.
Santos, W., Sousa, J.A., Gregorio, R., 2013. Thermal conductivity behaviour of polymers around glass and crystalline melting temperatures. Polym. Test. 32, 987–994.
Sarva, S., Mulliken, A.D., Boyce, M.C., 2007. Mechanics of Taylor impact testing of polycarbonate. Int. J. Solids Struct. 44, 2381–2400.
Schapery, R.A., 1984. Correspondence principles and a generalised J integral for large deformation and fracture analysis of viscoelastic media. Int. J. Fract. 25, 195–223.
Serban, D.A., Weber, G., Marsavina, L., Silberschmidt, V.V., Hufenbach, W., 2013. Tensile properties of semi-crystalline thermoplastic polymers: effects of temperature and strain rates. Polym. Test. 32, 413–425.
Sobieraj, M., Kurtz, S., Rimnac, C., 2009. Notch sensitivity of PEEK in monotonic tension. Biomaterials 30, 6485–6494.
Srivastava, V., Chester, S.A., Ames, N.M., Anand, L., 2010. A thermo-mechanically-coupled large-deformation theory for amorphous polymers in a temperature range which spans their glass transition. Int. J. Plast. 26, 1138–1182.
Triantafyllidis, N., Waldenmyer, J.R., 2004. Onset of necking in electro-magnetically formed rings. J. Mech. Phys. Solids 52, 2127–2148.
Vadillo, G., Rodríguez-Martínez, J.A., Fernández-Sáez, J., 2012. On the interplay between strain rate and strain rate sensitivity on flow localization in the dynamic expansion of ductile rings. Int. J. Solids Struct. 49, 481–491.
van Dommelen, J.A.W., Parks, D.M., Boyce, M.C., Brekelmans, W.A.M., Baaijens, F.P.T., 2003. Micromechanical modeling of the elasto-viscoplastic behavior of semi-crystalline polymers. J. Mech. Phys. Solids 51, 519–541.
Vladimirov, I.N., Pietryga, M.P., Reese, S., 2010. Anisotropic finite elastoplasticity with nonlinear kinematic and isotropic hardening and application to sheet metal forming. Int. J. Plast. 26, 659–687.
Wang, X., Shi, J., 2013. Validation of Johnson–Cook plasticity and damage model using impact experiment. Int. J. Impact Eng. 60, 67–75.
Wu, P.D., van der Giessen, E., 1995. On neck propagation in amorphous glassy polymers under plane strain tension. Int. J. Plast. 11, 211–235.
Xue, Z., Vaziri, A., Hutchinson, J., 2008. Material aspects of dynamic neck retardation. J. Mech. Phys. Solids 56, 93–113.
Yu, J.S., Maniatty, A.M., Knorr, D.B., 1997. Model for predicting thermal stresses in thin crystalline films. J. Mech. Phys. Solids 45, 511–534.
Zaera, R., Rodríguez-Martínez, J.A., Vadillo, G., Fernández-Sáez, J., 2014. Dynamic necking in materials with strain induced martensitic transformation. J. Mech. Phys. Solids 64, 316–337.
Zaïri, F., Naït-Abdelaziz, M., Gloaguen, J.M., Lefebvre, J.M., 2008. Modelling of the elasto-viscoplastic damage behaviour of glassy polymers. Int. J. Plast. 24, 945–965.